Investigating Limits of Ultra-low Emittance Photocathodes

by

Gevork Samvelovich Gevorkyan

A Dissertation Presented in Partial Fulfillment
of the Requirements for the Degree
Doctor of Philosophy

Approved June 2023 by the
Graduate Supervisory Committee:

Siddharth Karkare, Chair
Howard Padmore
Ricardo Alarcon
Robert Kaindl
William Graves

ARIZONA STATE UNIVERSITY

August 2023

ABSTRACT

Producing a brighter electron beams requires the smallest possible emittance from the cathode with the highest possible current. Several materials like ordered surface, single-crystalline metal surfaces, ordered surface, epitaxially grown high quantum efficiency alkali-antimonides, topologically non-trivial Dirac semimetals, and nano-structured confined emission photocathodes show promise of achieving ultra-low emittance with large currents. This work investigates the various limitations to obtain the smallest possible emittance from photocathodes, and demonstrates the performance of a novel electron gun that can utilize these photocathodes under optimal photoemission conditions.

Chapter 2 discusses the combined effect of physical roughness and work function variation which contributes to the emittance. This is particularly seen in polycrystalline materials and is an explanation for their higher than expected emittance performance when operated at the photoemission threshold. A computation method is described for estimating the simultaneous contribution of both types of roughness on the mean transverse energy. This work motivates the need for implementing ordered surface, single-crystalline or epitaxially grown photocathodes.

Chapter 3 investigates the effects of coulomb interactions on electron beams from theoretically low emittance, low total energy spread nanoscale photoemission sources specifically for electron microscopy applications. This computation work emphasizes the key role that image charge effects have on such cold, dense electron beams. Contrary to initial expectations, the primary limiter to beam brightness for theoretically ultra-low emittance photocathodes is the saturation current.

Chapters 4 and 5 describe the development and commissioning of a high accelerating gradient, cryogenically cooled electron gun and photoemission diagnostics beamline within the Arizona State University Photoemission and Bright Beams research

lab. This accelerator is unique in it's capability to utilize photocathodes mounted on holders typically used in commercial surface chemistry tools, has the necessary features and tools for operating in the optimal regime for many advanced photocathodes. A Pinhole Scan technique has been implemented on the beamline, and has shown a full 4-dimensional phase space measurement demonstrating the ability to measure beam brightness in this gun. This gun will allow for the demonstration of ultra-high brightness from next-generation ultra-low emittance photocathodes.

To my fiancée, Natalie Akram.

ACKNOWLEDGMENTS

As I prepare to graduate, I wish to express my deepest gratitude to those who have played a significant role in my life. First and foremost, I want to thank God for all He has done for me and continues to do for me each day. I want to thank my mother for being by my side, no matter what. I want to thank my father and his wife for being in support of my hard work and determination to reach my goals. Thank you to my brother, sister, and their spouses for always being there for me when I've needed them.

I give special thanks to my dear friends, many of whom helped shape my personality over the course of my PhD. I especially appreciate my pastor and the clergy of my church for being my home away from home all these years. I would like to acknowledge the funding support from the U.S. National Science Foundation funded the Center for Bright Beams and the Department of Energy, the work I've done would not have been possible without these organizations. I thank all the faculty and staff of the academic institutions and organizations that I've worked with, I will always cherish the kindness of your help and guidance. The most important of everyone is my advisor, Dr. Siddharth Karkare, who has been my greatest academic mentor. I've spent a fifth of my life working with you, it was a pleasure.

Lastly, I want to extend my heartfelt thanks to my beloved fiancée , who has been my inspiration to push myself beyond my limits and achieve my goals every day. Here is to a long and healthy future together.

TABLE OF CONTENTS

LIST OF FIGURES

Chapter 1

INTRODUCTION

The production of brighter electron beams can result in major advancements in x-ray sources like X-ray Free Electron Lasers (XFEL) [Emma *et al.* (2010); Pellegrini (2012)] and inverse Compton scattering experiments [Graves *et al.* (2014, 2009, 2012)]; ultrafast electron scattering techniques like Ultrafast Electron Diffraction (UED) and Ultrafast Electron Microscopy (UEM) [Wang *et al.* (2006); Hastings *et al.* (2006); Musumeci *et al.* (2010); Murooka *et al.* (2011); Li *et al.* (2009); Manz *et al.* (2015); Weathersby *et al.* (2015)], and Ultrafast Electron Energy Loss Spectroscopy (U-EELS) [Carbone *et al.* (2009); Pomarico *et al.* (2018)]; and particle colliders [National Academies of Sciences, Engineering, and Medicine (2018); Montag *et al.* (2021)] for fundamental physics research. For XFELs, a brighter electron beam from the source produces higher pulse energies and lasing photon energies[Wang *et al.* (2016)]. A brighter beam also enables the development of compact XFELs which fit inside a university laboratory, drastically increasing their accessibility and scientific reach[Rosenzweig *et al.* (2020)]. Achieving higher brightness also produces bunched electron beams with longer coherence lengths increasing the k-space resolution to enable the study of larger crystal structures at ultra-fast timescales, including moiré patterns[Li *et al.* (2022); Tran *et al.* (2019); Seyler *et al.* (2019); Brem *et al.* (2020); Duncan *et al.* (2022)] and complex molecular dynamics[Kabius *et al.* (2012)]. Brighter electron beams from the source, when transported to the sample through aberration-free/aberration-corrected electron optics, can enable vibrational spectroscopy with sub-angstrom spatial resolution and small energy resolutions simultaneously in an electron microscope. Brighter electron beams also result in higher luminosity in par-

ticle colliders enabling study of low-cross-section particle interactions [Witte *et al.* (2021)].

A beam's utility can be quantified by a single figure of merit called the brightness, which represents the beam's density in phase space and is inversely proportional to the transverse emittances. In this thesis we will investigate the various limitations to obtain the smallest possible emittance from a wide range of photocathodes. We will describe the development and commissioning of a novel electron gun which was built to utilize these photocathodes under optimal photoemission conditions. We also demonstrate the performance of this electron gun and the corresponding beamline by implementing an emittance measurement technique, indicating that this tool be used to demonstrate ultra-high brightness from next-generation ultra-low emittance photocathodes.

1.1 Quantifying Beam Brightness and Emittance

For the electron based tools previously mentioned, the key figure of merit is the 5D beam brightness [Ruska (1933); Brau (2003)]. This brightness is typically used for photoemission based linear electron accelerators, or photoinjectors, with low longitudinal and transverse coupling [Musumeci *et al.* (2018)].

$$B_{5D} = \frac{2I}{\pi^2 \epsilon_\mathrm{x} \epsilon_\mathrm{y}}, \tag{1.1}$$

where I is the electron beam current and ϵ_i is the normalized RMS transverse emittance. The emittance is defined as

$$\epsilon_{ni} = \frac{1}{m_0 c} \sqrt{\langle x^2 \rangle \langle p_x^2 \rangle - \langle x p_x \rangle^2}, \tag{1.2}$$

where m_0 is the electron mass, c is the speed of light, x represents position, and p_x represents momentum. The normalized RMS emittance represents the area that the

beam occupies in phase space; it is a measure of the size, the momentum spread, and the position-momentum correlation of the beam. This can be rewritten as

$$\epsilon_{ni} = \sigma_i \sqrt{\text{MTE}/m_0 c^2}, \tag{1.3}$$

where σ_i is the laser beam spot size. The term MTE is the mean transverse energy, equal to

$$\frac{1}{2} m_0 v_\perp^2, \tag{1.4}$$

where $v_\perp$ is the electron velocity in the direction transverse to the beam propagation. This can be thought of as the "temperature" of the beam. In applications not dominated by space charge, the photoemission area is nearly the same as the laser beam spot size. However in applications involving pulsed electron beams (excluding single-shot or stroboscopic techniques) where the number of particles per RMS beam area is proportional to the electric field [Filippetto *et al.* (2014)], we can use equation 1.3 to describe a 4D beam brightness.

$$B_{4D} = \frac{m_0 c^2 E_0^n}{2\pi \text{MTE}}, \tag{1.5}$$

where E_0 is the accelerating electric field at the photocathode surface at the time of electron emission, and n is a number between 1 (pancake beams) and 2 (cigar beams) depending on the shape of the electron bunch [Musumeci *et al.* (2018)]. Endeavors to increase the brightness by creating higher electric fields have been very successful with RF guns, and active efforts continue improve the photoinjector technology [Arnold and Teichert (2011)]. Reducing the MTE is another option for obtaining higher brightness beams, and this requires a vast overhaul in the approach toward next generation photoinjectors such that advanced photocathodes can be implemented in optimal photoemission regimes.

1.2 Photoemission Effects that Limit the MTE

While the maximum electric field is limited by the design of the electron gun and electric breakdown, the MTE is limited by the photocathode material – its surface and the laser used for electron emission. In figure 1.1 we show a three-step model of photoemission by Dr. Dowell and Dr. Schmerge [Dowell and Schmerge (2009)].
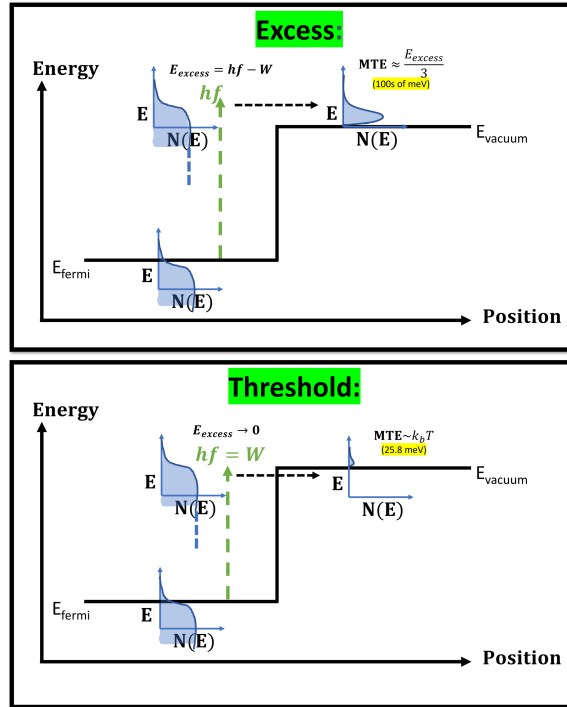
Figure 1.1: Dowell's model of the photoemission process says that photons excite electrons, and those electrons with energy above the work function escape into vacuum. In the case where the photon energy is greater than the work function (Excess), the MTE proportional to that excess energy. When the photon energy is equal to or slightly less than the work function (Threshold), only the tail end of the Fermi distribution overcomes the work function and the MTE is proportional to the photocathode lattice temperature.

Electrons from the conduction band are excited by an incoming photon and emitted into vacuum. For photocathodes with disordered surfaces MTE is proportional to the excess energy, E_{ex}, which is the difference between the photon energy and the

photocathode work function:

$$\text{MTE} \approx E_{ex}/\alpha. \tag{1.6}$$

In this equation α is generally equal to 3 for ideal metals, but can vary because of several factors such as the band structure and electron scattering during emission [Dowell and Schmerge (2009)]. By tuning the photon energy to the work function such that the excess energy is zero or slightly negative, electrons are emitted from the tail of the Fermi distribution resulting in MTE being limited by thermal energy.

$$\text{MTE} \approx k_B T, \tag{1.7}$$

where T indicates the photocathode lattice temperature and k_B indicates the Boltzmann constant [Vecchione et $al.$ (2013)]. Operating in the threshold photoemission regime to produce lower MTE comes at the cost of producing less current. For a simple free electron metal, where most of the scattered electrons do not get emitted, the quantum efficiency (QE) is quadratically related to the excess energy; for example, reducing from an excess energy typical of today's photoinjectors (around 0.5 eV) to threshold would result in a factor of 400 lower QE.

The atomically ordered surface of Ag(111), operating at 0.15 eV above threshold, demonstrated an MTE as low as 25 meV at room temperature with QE as high as 10^{-4} [Karkare et $al.$ (2017)] by utilizing the low effective electron mass of the Ag(111) surface state. An MTE as low as 5 meV was measured via near-threshold photoemission from the cryogenically cooled, atomically ordered surface of Cu(100) [Karkare et $al.$ (2020)], however the QE was expected to be quite low ($\langle 10^{-8}$). In principle, it is possible to compensate the deficit in the bunch charge due to a lower QE by increasing the laser pulse energy, up to the point where direct electron heating in the solid and non-linear photoemission becomes significant [Maxson et $al.$ (2016); Knill et $al.$ (2021)].

Another way is to use high QE semiconductor photocathodes like alkali-antimonides or III-V semiconductors activated to negative electron affinity. Such materials have a large QE since a large fraction of the scattered electrons do get emitted [Karkare *et al.* (2013); Jensen (2013)]. Alkali-antimonides have shown a lot of promise as high QE and low MTE materials; they have already been demonstrated to produce an MTE at the room temperature thermal limit [Feng *et al.* (2015)]. So far an MTE smaller than 22 meV – along with a QE as high as 7×10^{-5} – has been measured from alkali-antimonide based photocathodes at liquid nitrogen temperatures close to the photoemission threshold [Cultrera *et al.* (2015b)]. Other factors such as many-body scattering with phonons [Nangoi *et al.* (2021)], non-linear photoemission [Knill *et al.* (2021)], and lattice defect states [Cultrera *et al.* (2015a)] affect the MTE as well.

Photoemission sources used in existing photoinjectors and UED applications typically use polycrystalline metal or high QE semiconductor photocathodes with a conveniently available laser wavelength to obtain electrons with MTE in the few 100 meV range [Musumeci *et al.* (2018)]. For stroboscopic UED applications, the RMS source size is limited by the smallest possible diffraction limited spot size that the photoemission laser can be focused to on the photocathode surface and is typically of the order of 5 μm, thus, resulting in an emittance of a couple of nm-rad [Li *et al.* (2012)]. Reducing this emittance further will require reduction of the MTE and reduction of the photoemission spot size.

In chapter 2 of this dissertation, we discuss another MTE increasing effect pertaining to polycrystalline photocathodes due to nanoscale physical roughness and work function variations. We describe a technique to calculate the electric fields close to a surface exhibiting real physical and chemical roughness measurements from our atomic force microscope (AFM) and kelvin-probe force microscope (KPFM). We numerically calculate the trajectories of electrons in these fields and calculate the

expected MTE variation with the accelerating gradient due to the combined effect of physical and chemical roughness. We show that for a real alkali-antimonide surface the combined effect of physical and chemical roughness would initially cause the MTE to reduce with increasing electric field, go to a minimum and then increase again. This suggests the need for atomically ordered, single-crystalline or epitaxially grown photocathodes.

Then in chapter 3 we investigate the effects of coulomb interactions on electron beams from theoretically low MTE, low energy spread nanoscale photoemission sources specifically for electron microscopy applications. This computation work emphasizes the key role that image charge effects have on such cold, dense electron beams. Contrary to initial expectations, the MTE and RMS total energy spread are preserved as the laser spot size is decreased to the nanoscale. The primary limiter to beam brightness then becomes the saturation current.

In chapter 4 we address the need for of a photocathode test bed accelerator by detailing the development and commissioning of a high accelerating gradient, cryogenically cooled, 200 kV DC electron gun within our photocathodes research lab. This gun is unique in its capability to utilize photocathodes mounted on holders typically used in commercial surface chemistry tools. This electron gun is able to operate vibration-free at crygenic temperatures, is directly connected under ultra-high vacuum (UHV) to a photocathode growth chamber and multiple photocathodes diagnostic chambers, and has access to the necessary surface preparation tools and a tunable wavelength laser for operating in the optimal regime for many advanced photocathodes.

In chapter 5 we describe the beamline connected to this electron gun, along with the type of photoemission diagnostic measurements we plan to implement. We describe a full 4D phase space measurement technique, and we demonstrate this tech-

nique with the first emittance measurements using our electron gun with an alkali-antimonide (Cs_3Sb) photocathode grown on a molybdinum substrate. Recent developments in molecular beam epitaxy have demonstrated the growth of epitaxial Cs_3Sb on lattice matched silicon carbide [Parzyck *et al.* (2022)], so these materials exist and can be grown. The future plan is to investigating these types of advanced photocathodes in this electron gun. The future development of the beamline will including adding a 3.0 GHz deflection cavities to enable response time measurements. Finally, we intend to add a 3.0 GHz bunching cavity for longitudinal phase space manipulation, which will allow us to perform UED with ultra-low emittance photocathodes.

Chapter 2

EFFECTS OF SURFACE ROUGHNESSES ON MTE

ABSTRACT

With ongoing improvements in photocathode design and synthesis, we are now at a point where the physical and chemical surface roughness of the photocathode can become a limiting factor. Here we show how measurements of the spatially dependent variations in height and surface potential can be used to compute the electron beam mean transverse energy, one of the key determining factors in evaluation of brightness. This chapter extends Gorlov's formalism to model electric fields close to physically rough surfaces by using a spectral method to include the varying surface potential. Then the evolution of a uniform electron beam is tracked using the computed electric fields, omitting space charge effects. The result is a lower bound for the contribution of mean transverse energy from nanoscale surface roughness, which can be as high as the thermal contribution when evaluating polycrystalline photocathodes.

2.1   Introduction

The photocathode in a photoinjector is immersed in a strong longitudinal electric field gradient typically in the range $5 - 100$ MV/m. If a small area of the surface is tilted due to local roughness, this will produce a transverse electric field gradient which will increase the MTE correlated to the magnitude of the applied electric field. The effect will depend on the local tilt of the surface such that nanoscale surface height variations, if accompanied by a relatively small periodicity, can produce large effects on the MTE. In addition, most photocathodes used today are polycrystalline, and these photocathodes will exhibit changes in local work function depending on their chemical composition and the local orientation of the surface. This effect is particularly significant in multi-element photocathodes, such as the alkali-antimonides, due to local changes in stoichiometry [Xie *et al.* (2017)].

Due to their high QE even at photon energies close to threshold, alkali-antimonides are one of the few materials capable of delivering ultra-low emittance electron beams with large bunch charges. Although co-deposition methods have reduced the physical roughness and the extent of local changes in potential in alkali-antimonides [Karkare *et al.* (2018)], it is common to find height variations of a few nm and chemical potential amplitudes of 0.1 V over length scales of $50 - 200$ nm.

These variations can be measured quite accurately using Atomic Force Microscopy (AFM) and Kelvin Probe Force Microscopy (KPFM). As we advance from an MTE of several hundred meV to the few meV range, we will need to find ways to control both forms of local variation. The aim of this work is to demonstrate a method to use measured photocathode surface roughness and potential variations to predict the ultimate MTE limited by the surface non-uniformities that can be achieved for a defined accelerating gradient for the particular photocathode.

Previously, several authors have calculated the effects of physical roughness on MTE [Martinelli (1973); Krasilnikov (2006); Jensen *et al.* (2014)] using various approaches. Here we discuss the works that are most relevant to our approach. Bradley developed an analytic expression for the MTE from a 1-D sinusoidal surface variation for the case where the amplitude of the variation was much smaller than the period [Bradley *et al.* (1977)]. This approximation to the electric field was used to estimate increase in emittance due to a sinusoidal physical roughness accurately [Xiang *et al.* (2007)]. Zhang and Tang extended this formalism to 2-D surfaces with realistic surface roughness by expanding the surface in terms of its Fourier coefficients [Zhang and Tang (2015)]. Gorlov used a more precise and combined analytic numerical method of the 3-D field calculation close to a realistic 2-D surface [Gorlov (2007)]. This method has been used to obtain the MTE increase from the physical roughness on realistic photocathode surfaces measured using an AFM [Feng *et al.* (2017); Karkare and Bazarov (2011)]. Despite the varying complexity of these studies, all of them conclude that the MTE increase due to the physical roughness.

$$\text{MTE}_{\text{physical}} = \frac{\pi^2 a^2 E_0 |e|}{2\lambda}, \tag{2.1}$$

where a and λ are the surface height peak and periodicity respectively, E_0 represents the accelerating electric field at the photocathode surface, and $|e|$ is the electron charge.

More recently Karkare and Bazarov have investigated the effects of chemical roughness or varying surface potentials on the MTE from surfaces with no physical roughness [Karkare and Bazarov (2015)]. In this investigation they showed that MTE will increase due to the varying surface potential.

$$\text{MTE}_{\text{chemical}} = \frac{\pi^2 h^2 |e|}{4\sqrt{2}aE_0}, \tag{2.2}$$

where h is the amplitude of the work-function variation and a is its spatial period. They showed that surface potential variations as small as 100 mV over 100 nm can cause MTE increases as large as 30 meV. For larger accelerating electric fields, the MTE reduces with increasing accelerating field. For smaller accelerating electric fields, the MTE remains constant due to the influence of the varying surface potential.

Real photocathode surfaces can exhibit both physical and chemical roughness simultaneously. The physical roughness tends to increase the MTE with increasing accelerating gradient whereas the effect of chemical roughness on MTE diminishes with increasing accelerating gradient. Hence predicting the combined effect of both on the MTE as a function of accelerating gradient is non-trivial.

In this chapter, based on Gorlov's method of calculating the electric potential, we describe the technique we developed to calculate the electric potential and fields close to a surface exhibiting realistic physical and chemical roughness [Gevorkyan *et al.* (2018). This technique can use AFM and KPFM measurements of real photocathode surfaces as inputs to calculate the electric fields close to the surface for any given accelerating gradient. As a demonstration, we calculate the electric fields close to the surface of an alkali-antimonide photocathode measured using AFM and KPFM. Then, we numerically calculate the trajectories of electrons in these fields and calculate the expected MTE variation with the accelerating gradient due to the combined effect of physical and chemical roughness. We show that for a real alkali-antimonide surface the combined effect of physical and chemical roughness would initially cause the MTE to reduce with increasing electric field, go to a minimum and then increase again. All computation work has been conducted using MATLAB®.

2.2   Calculation of Electric Fields Close to the Surface

2.2.1   Description of the Method

To track a single electron through space close to the photocathode surface, we need to have an accurate model of the electric field at all positions. In principle, any finite element or boundary element method can work for this calculation, however due to the small scale of the surface roughness relative to the spatial scale of the problem, these methods become impractical owing to large computational requirements. To circumvent this issue, Gorlov suggested a formalism based on modeling the electric potential using a combination of sinusoidal and exponential functions and applied it to an equipotential surface with nano-scale physical roughness [Gorlov (2007)]. Here we extend Gorlov's formalism to model electric fields close to physically rough surfaces with varying surface potential.

We model this problem using a parallel-plate capacitor where one plate is the physically rough photocathode with varying surface potential (generally obtained from an AFM and KPFM measurement) and the other plate is flat and held at a distance L_0 away from the photocathode at a potential Φ. Figure 2.1 is a drawing that roughly sketches this model and the equipotential lines produced in between the plates. The distance L_0 is chosen such that it is much larger than the lateral x, y dimensions of the measured surface and the maximum amplitude of the physical roughness. This model assumes that the photocathode surface is infinite in the x and y directions with periodic images of the measured surface.

To calculate the electric potential between the two plates, let us assume that the lengths of the measured surface in the x and y directions are L_x and L_y respectively. Let us assume that the measured surface height is given by $f(x, y)$ and the measured surface potential is given by $U_0(x, y)$. Now the problem reduces to solving the

13
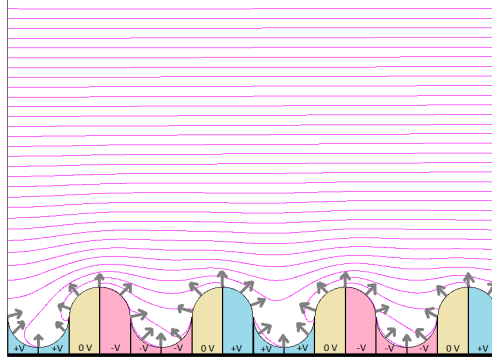
Figure 2.1: Parallel-plate model to simulate equipotential lines produced by surface and chemical roughness. The gray arrows represent electrons emitted from the photocathode. The blue regions show areas with positive surface potential, the beige regions show areas with zero surface potential and the red regions show areas with negative surface potentials. This image is only meant to describe the model used to solve the problem and a rough depiction of the equipotential lines close to a surface with physical and chemical roughness and does not depict a real photocathode surface used for simulations in this chapter.

Poisson's equation $\nabla^2 U = 0$ for the potential $U(x, y, z)$ under the following boundary conditions:

$$U|_{z=L_0} = \phi \tag{2.3}$$

$$U(x + L_x, y + L_y) = U(x, y) \tag{2.4}$$

$$U|_{z=f(x,y)} = U_0(x, y) \tag{2.5}$$

One ansatz for $U(x, y, z)$ that satisfies the Poisson equation and the boundary conditions given by 2.3 and 2.4 is:

14

$$U = \sum_{m_1,n_1=0}^{N} c_{m_1,n_1} K \cos\left(\frac{2\pi}{L_x}m_1 x\right) \cos\left(\frac{2\pi}{L_x}n_1 y\right) \tag{2.6}$$

$$+ \sum_{m_2,n_2=0}^{N} c_{m_2,n_2} K \cos\left(\frac{2\pi}{L_x}m_2 x\right) \sin\left(\frac{2\pi}{L_x}n_2 y\right)$$

$$+ \sum_{m_3,n_3=0}^{N} c_{m_3,n_3} K \sin\left(\frac{2\pi}{L_x}m_3 x\right) \cos\left(\frac{2\pi}{L_x}n_3 y\right)$$

$$+ \sum_{m_4,n_4=0}^{N} c_{m_4,n_4} K \sin\left(\frac{2\pi}{L_x}m_4 x\right) \sin\left(\frac{2\pi}{L_x}n_4 y\right)$$

$$+ \frac{\varphi z}{L_0}$$

Where $K = \frac{e^{-\gamma z} - e^{(z-2L_0)\gamma}}{1-e^{-2L_0\gamma}}$, $\gamma = 2\pi\sqrt{\left(\frac{m}{L_x}\right)^2 + \left(\frac{n}{L_y}\right)^2}$. By using the assumption that the anode distance $L_0 \gg \max(f(x,y))$, L_x and L_y, we reduce the exponential term of the coefficient K to be $K \approx e^{-\gamma z}$. Equation 2.6 can be written in a more concise manner as:

$$U = \sum_{n=1}^{4(N+1)^2} c_i \times \phi_i(x,y) \tag{2.7}$$

where c_i are the coefficients (either of c_{m_1,n_1}, c_{m_2,n_2}, c_{m_3,n_3} or c_{m_4,n_4}) for the various corresponding basis functions ϕ_i (the four listed in equation 2.6.

Now the problem reduces to finding the coefficients c_i corresponding to the basis functions ϕ_i such that the boundary condition given by equation 2.5 is satisfied. Note that the basis functions ϕ_i are not orthonormal as they contain the exponential term K in order to satisfy the Poisson equation. Here we use the Ritz method [Gorlov (2007)] to find the set of coefficients c_i that minimizes the difference between the measured surface potential $U_0(x,y)$ and the potential obtained from equation 2.7 over the surface. This difference ε is given by:

$$\varepsilon = \left(\iint_S (\xi)^2 \, dx dy\right)^{1/2} \tag{2.8}$$

15

where S is the surface $y = 0$ to L_y and $x = 0$ to L_x, and $\xi = U_0(x,y) - \sum_{i=1}^{4(N+1)^2} c_i \cdot \phi_i(x,y,f(x,y))$. By differentiating ε^2 with respect to each c_i coefficient and setting the derivatives to zero, we obtain series of $4(N+1)^2$ equations with the c_i coefficients as unknowns. This series of equations can be expressed in the form of a matrix equation as:

$$\vec{B} = \mathbf{A} \cdot \vec{C} \tag{2.9}$$

where $\vec{B}$ is a vector of length $4(N+1)^2$ with elements given by:

$$b_j = \iint_S U_0(x,y) \cdot \phi_j(x,y) dx dy \tag{2.10}$$

$\mathbf{A}$ is a $4(N+1)^2 \times 4(N+1)^2$ matrix with elements given by

$$a_{ij} = \iint_S (\phi_i(x,y) \cdot \phi_j(x,y) dx dy \tag{2.11}$$

and $\vec{C}$ is a vector with elements c_i. The vector $\vec{C}$ can then be calculated by inverting the A matrix and is given by $\vec{C} = \mathbf{A}^{-1}\vec{B}$. Once the c_i coefficients are known, $U(x,y,z)$ can be analytically computed from equation 2.7. The electric field can also be calculated by differentiating the potential U. If the basis functions φ were orthonormal, A would be exactly the identity matrix and $\vec{B}$ would be equal to $\vec{C}$, resulting in a standard Fourier transformation.

2.3   Validation

We verify the validity of the above formalism by comparing its results to those obtained from various sources with well-defined potentials. First we compare the results obtained by the above formalism to those obtained by Bradley [Bradley *et al.* (1977)] for an equipotential surface with a 1-D sinusoidal variation. Bradley analytically calculated the transverse (x) and longitudinal (z) fields for an equipotential surface given by $z = a \cdot \cos(px)$, placed in an electric field of strength E_0 to first order

16

under the assumption $a \ll p$. The electric fields are as follows:

$$E_x = E_0 a p \cdot e^{-pz} \cdot \sin(px) \qquad (2.12)$$

$$E_z = E_0 + E_0 a p \cdot e^{-pz} \cdot \cos(px) \qquad (2.13)$$
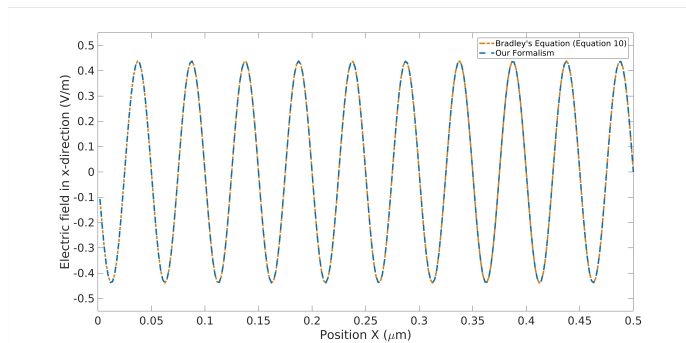
(a) Electric field in x-direection
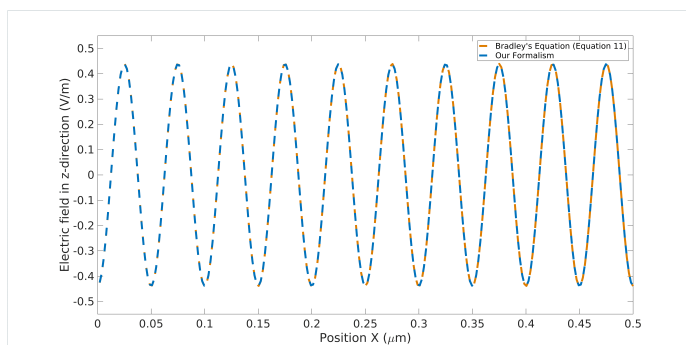
(b) Electric field in z-direction

Figure 2.2: Comparison of electric fields i n x -direction (2.2a) a nd i n z-direction (2.2b) 100 nm away from a 1D sinusoidal surface as calculated using Bradley's equations (orange dashes) and using the formalism presented here (blue dashes). The z-direction is plotted with the constant electric fields r emoved. T hey m atch o ne another to within three significant digits.

In figure 2 .2 w e c ompare t he e lectric fi elds co mputed by ou r fo rmalism against Bradley's formulas. Using inputs of $E_0 = 1.0$ MV/m, $a = 1.0$ nm, and $p = 2\pi/50$ nm^{-1}, we modeled the electric fields a t t he s ource s urface. F or t his s ource, t he simulated surface size was 500 nm × 500 nm sampled on a equispaced mesh of size 256×256. The surface is assumed to be equipotential. The fields are evaluated on the plane

z = 100 nm above the photocathode surface. The distance was chosen arbitrarily to verify the accuracy of the model near the surface.

As seen in figure 2.2, our formalism produces electric fields identical to those obtained from Bradley's equations with an accuracy down to three significant digits. The RMS difference of the electric fields were 5.67×10^{-4} V/m for both the x-direction and z-direction. The small phase discrepancy in the results comes from the lack of higher order terms in Bradley's solution.

To check the validity of this method for a surface with varying surface potential, we utilized electric potential solutions published by Karkare and Bazarov [Karkare and Bazarov (2015)] to examine a surface with constant height but sinusoidally varying surface potential. Using the same general parameters as before, we set the surface height to be constant and vary the surface potential as $U_0(x, y) = h \sin(p_X x) \cdot \sin(p_y y)$. For such a surface placed in an external electric field of strength E_0 the potential near the surface is analytically given by:

$$U(x, y, z) = E_0 z + h e^{-\gamma z} \cdot \sin(p_x x) \cdot \sin(p_y y) \tag{2.14}$$

where E_0 is the applied external electric field, h is the amplitude of the surface potential variation and $\gamma = \sqrt{p_x^2 + p_y^2}$. As with the previous case, we set the applied electric field as 1.0 M V/m. We used a surface potential amplitude $h = 0.5$ V, and frequencies $p_x = p_y = 2\pi/50$ nm^{-1}. Using the another arbitrary distance close to the surface, the plots in figure 2.3 compare the potential U at z = 10 nm above the surface when computed using equation 2.14 and when computed via our formalism. The RMS difference of the calculated using the two methods is 0.0014 V which is about 1.6%.

It can be seen that our formulation, from equation 2.7, reduces to Bradley's and Bazarov's results for the surface variations that they have considered respectively. This formulation provides a more general result that can be applied to a surface with

18
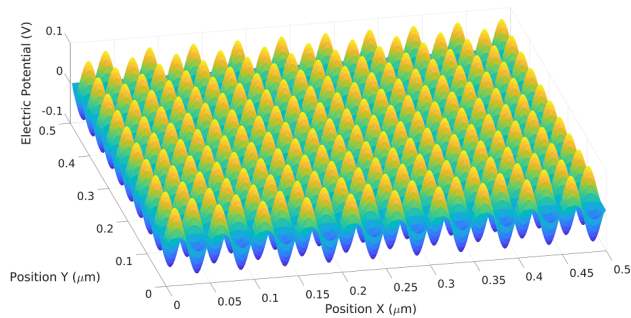
(a) Electric potential from Eq. (12)
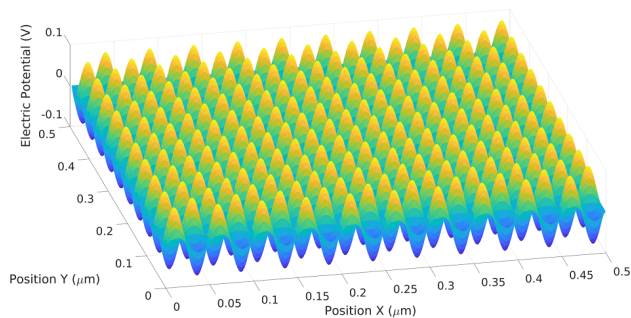
(b) Electric potential from our formalism

Figure 2.3: Comparison of the electric potential computed 10 nm above a uniform photocathode surface with 2D sinusoidally varying surface potential using (2.3a) equation 2.14 as obtained from [Karkare and Bazarov (2015)] and (2.3b) using the formalism presented in this chapter. The offset term of the electric potential is subtracted to show the variation. The two match to within 1.6%.

any physical and potential variation and thus will be very useful to investigate real photocathode surfaces.

2.4 MTE Calculation for an Alkali-Antimonide Surface

A Cs_3Sb photocathode was grown in a UHV growth chamber using the co-deposition technique. The details of the growth are given elsewhere [Feng *et al.* (2017)]. The photocathode was then transferred into an Atomic Force Microscope (AFM) with the Kelvin Probe Force Microscopy (KPFM) capability [Melitz *et al.* (2011)] under UHV conditions. Surface height and potential maps were measured for this photocathode surface using the AFM and KPFM techniques respectively.
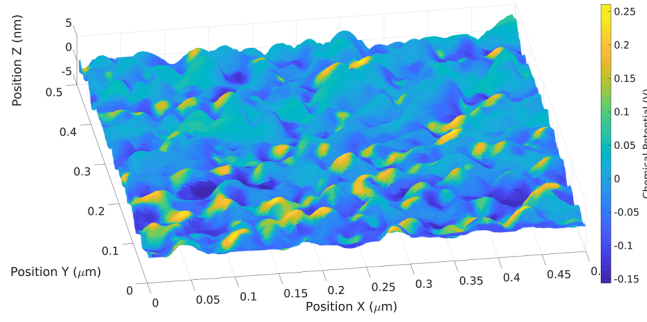
(a) AFM with KPFM surface potential
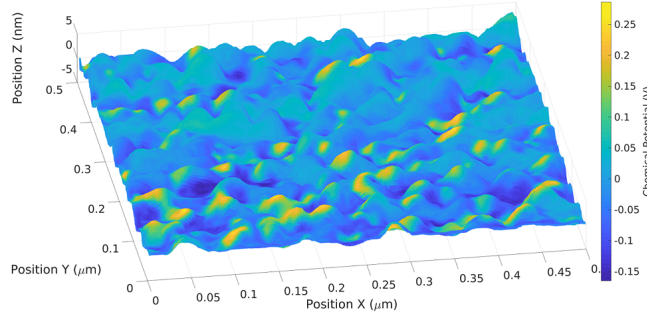
(b) AFM with computed surface potential

Figure 2.4: Surface physical and chemical roughness of Cs_3Sb as measured by AFM and KPFM (2.4a). Surface potential as calculated by our formalism on the rough surface (2.4b). The color coding denotes the potential variation on the surface.

The measured surface map is shown in figure 2.4a. Note that these measurements are only preliminary and are used here as an example of a physically and chemically rough surface. Detailed results from these measurements will be published elsewhere. The electric potential of the surface is reproduced and plotted on the surface in figure 2.4b using our formalism. For this surface we obtain an RMS error ϵ = 9.96 mV, which is a fractional error of 2.2%. The RMS error depends upon the sampling rate, sample size of the surface (L_x, L_y), the number of frequencies N used in our formulation, the periodicities of surface roughness, and the amplitudes of surface height and potential variation. The larger is the number of frequencies used, the smaller is the RMS error. However, this formalism becomes numerically unstable for very large frequencies [Gorlov (2007)].

Utilizing the derived electric fields computed using the above formalism for the measured surface height and potential maps, we simulated the trajectory of electrons as they would be accelerated away from such a photocathode surface placed in an accelerating electric field. The electrons were tracked until the effects of the surface height and potential variations become negligible. We use a symplectic Velocity Verlet [Swope *et al.* (1982)] tracker for this purpose. Electrons were launched from a uniform 100×100 (x,y) grid on the surface with zero kinetic energy. The number of frequencies used to calculate the electric fields (N) was set to 45 and the time increment for electron trajectory calculation was set to 5.0 fs. The time step was chosen to be small enough that doubling the time step did not change any of the electron trajectories significantly.

The MTE of these electrons was calculated as the average transverse kinetic energy of all the electrons after they are far enough from the surface that the electric fields due to the surface height and potential variations are negligible. This gives an estimate of the surface variation contribution to the MTE from a real photocathode surface.
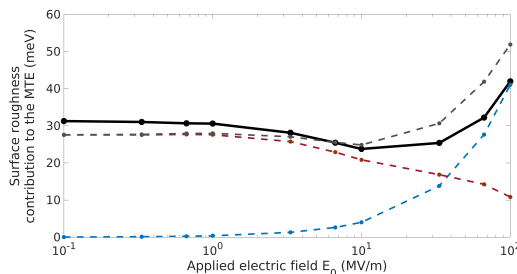
Figure 2.5: Surface non-uniformities contribution to the mte from the Cs_3Sb photocathode surface shown in figure 2.4 (solid black line). At lower electric fields the MTE is dominated by the variations in surface potential, whereas, at higher electric fields it is dominated by the physical surface roughness. This figure also shows the MTE obtained from the surface assuming only potential variations and no height variations (red dotted line), assuming only height variations and a constant potential (blue dotted line) and the sum of the two (gray dotted line). Despite the same surface potential on the surfaces corresponding to the solid black line and the dashed gray/red line, the 3 meV difference in MTE at zero electric field arises due to the fact that these surfaces have a different physical roughness and hence different surface electric fields despite the same surface potential.

The calculated MTE as a function of the accelerating electric field is shown in figure 2.5 (black solid line). This plot also shows the MTE obtained from the surface assuming only potential variations and no height variations (red dotted line), assuming only height variations and a constant potential (blue dotted line) and the sum of the two (black dotted line). It is clear that a simple addition of the MTE obtained from a surface with only potential variation and a surface with only height variations is not equal to the MTE calculated from a surface which has both the potential and height variations simultaneously.

At smaller accelerating electric fields, the contribution of height variations is negligible, however the MTE is dominated by the surface potential variations. This contribution remains nearly invariant at a value of ≈ 31 meV until the electric field exceeds 1 MV/m after which it reduces with increasing electric field. This reduction is expected because, as the accelerating field increases the electrons spend a smaller time in the region with significant transverse electric fields due to surface potential changes. The contribution of the surface height variation to the MTE is proportional to the accelerating electric field. Hence, as the accelerating electric field is increased further, the MTE reaches a minimum and starts to increase with the accelerating electric field.

We note here that figure 2.5 shows only the surface non-uniformities contribution to the MTE. In reality, several other factors like the photocathode lattice temperature, photon energy in excess of the work function and the electronic band-structure of the photocathode materials also contribute significantly to the MTE. In principle, by cryogeincally cooling the photocathode and by tuning the photon energy very close to the photoemission threshold, it should be possible to minimize the contributions of all these factors to a point where only the contribution of surface non-uniformities will be significant. The low field limit of MTE is significantly above the value for

k_BT at room temperature (≈ 25 meV), but reduces to approximately this value at the optimum accelerating field, around 10 MV/m. It should also be noted that various factors like non-uniform emission from the surface due to non-uniform work function and the initial kinetic energy distributions of the electrons have been ignored in this calculation. Including these effects will be a subject of future work.

The roughness contribution to the MTE calculated here at low electric fields is 32 meV. This is already much larger than the MTE of 22 meV measured from co-deposited Cs_3Sb at 90K temperature at the photoemission threshold [Cultrera *et al.* (2015)]. One reason for this discrepancy could be that the surface of the photocathode used to measure the MTE was significantly smoother than the surface shown in figure 2.4. This discrepancy underscores a need for complete surface characterization along with MTE measurements on the same photocathode surface.

2.5 Conclusion

Advancements in co-deposition methods of alkali-antimonide thin films have reduced the physical roughness and the extent of local changes in chemical potential significantly. Today, alkali-antimonide photocathodes with height variations of a few nm and chemical potential amplitudes of 0.05 V over length scales of $50 - 200$ nm [Karkare *et al.* (2018)] can be grown using these co-deposition methods. Such variations can, in principle, be measured accurately using AFM and KPFM. We developed a MATLAB® based program which allows us to calculate a lower bound to the MTE due to such surface variations at various accelerating electric fields. This knowledge is essential to understand the effects of photocathode surface variations on MTE and develop photocathodes that minimize these effects to obtain MTE well below the room temperature thermal limit.

We showed how the electric fields close to any rough surface with varying sur-

face potential can be calculated accurately using a spectral expansion. We verified the computational accuracy of the formalism using simulated surfaces with known analytic solutions to the electric fields. Then we calculated the contributions of the surface (physical and chemical) non-uniformities by launching electrons from the surface and numerically tracing their trajectories in the calculated electric fields close to the surface. We showed that for a co-deposited alkali-antimonide surface, the surface potential variations can limit the MTE at low electric fields to around 30 meV. At higher electric fields the contributions of the surface potential reduce and the MTE goes to a minimum. At even higher electric fields, the effects of physical surface roughness dominate the MTE, increasing it again.

In this work, we assumed that the electrons have no initial kinetic energy and "float" away from the surface under the influence of the applied and surface electric fields. This is partly valid if the photon energy is less than the work function, and the photocathode is cryogenically cooled to liquid helium temperatures. Then the initial velocity of each electron would be near zero, but would vary due to the chemical potential. The number of higher energy electrons would reduce exponentially with the tail of the Fermi distribution. In such a scenario, we can reasonably assume that all electrons are emitted with zero kinetic energy, and weighing the electrons with by a factor of $e^{-\frac{U_0}{kT}}$, where U_0 is the surface chemical potential, can be sufficient.

A more accurate way to incorporate the effects of surface and chemical roughness on the number and initial energy of electrons would be to emit electrons with distributions of energies, at distributions of angles, from each point respectively. The energy distributions would depend on the photon energy and the local surface potential. One feasible way to address this is to use a Monte-Carlo based approach to sample the energy and angular space. The hope is that even a dilute sampling of electron energies and angles from each spatial point would result in a statistically accurate MTE

when sampled over the entire surface. Further work on this program should work to remove the initial zero kinetic energy and the uniform electron emission assumptions.

These developments on the program would allow us to characterize the statistical nature of the emission in the far field. If we have a range of surface potentials close to the average threshold, then only the areas of low chemical potential will emit. The result will be an uneven far field distribution of electrons; and such speckling in the positional distribution would have an effect on the evolution of space charge. The aftermath would not be correlated space charge; it would represent an uncorrectable space charge limited MTE, and the program in its current form will not calculate these effects. However, we can use this program give us some idea of the speckle introduced in the electron beam due to surface non-uniformities. This speckle pattern can then be used as an input to other beam dynamics codes that allow the calculation of space charge effects.

The ideal photocathode would avoid complications from roughness entirely; that is another motivator to investigate photoemission from ordered surface, single-crystalline or epitaxially grown photocathodes. The potential limits of such ideal photocathodes are explored in chapter 3. Methods for synthesizing candidate photocathodes with atomically smooth, flat [Saha *et al.* (2022)] and ordered surfaces [Parzyck *et al.* (2022)] are in development and have shown success. These methods require growing these films on single-crystalline, lattice-matched substrates and show promise of obtaining MTEs below the thermal limit along with QE in the 10^{-3} range or better, allowing mitigation of nonlinear photoemission effects for large charge densities. Future improvements are expected from advanced single-crystalline photocathodes like topological insulators and Dirac semimetals [Musumeci *et al.* (2018)]. A tool built for such testing such materials is described in chapters 4 and 5.

2.6 Acknowledgements

REFERENCES

Bradley, D. J., M. B. Allenson and B. R. Holeman, "The transverse energy of electrons emitted from gaas photocathodes", J. of Phys. D **10**, 111 (1977).

Cultrera, L., S. Karkare, H. Lee, X. Liu, I. V. Bazarov and B. Dunham, "Quantum efficiency and thermal emittance of metal photocathodes", Physical Review Special Topics - Accelerators and Beams **18**, 113401 (2015).

Feng, J., S. Karkare, J. Nasiatka, S. Schubert, J. Smedley and H. A. Padmore, "Near atomically smooth alkali antimonide photocathode thin films", J. Appl. Phys. **121**, 044904 (2017).

Gevorkyan, G. S., S. Karkare, S. Emamian, I. V. Bazarov and H. A. Padmore, "Effects of physical and chemical surface roughness on the brightness of electron beams from photocathodes", Phys. Rev. Accel. Beams **21**, 093401, URL `https://link.aps.org/doi/10.1103/PhysRevAccelBeams.21.093401` (2018).

Gorlov, T., "High-precision calculation of quasistatic field near a photocathode surface microrelief", J. Electrostat **65**, 735 (2007).

Jensen, K. L., D. A. Shiffler, J. J. Petillo, Z. Pan and J. W. Luginsland, "Emittance, surface structure, and electron emission", Phys. Rev. ST Accel. Beams **17**, 043402 (2014).

Karkare, S. and I. V. Bazarov, "Effect of nanoscale surface roughness on transverse energy spread from gaas photocathodes", Appl. Phys. Lett. **98**, 094104 (2011).

Karkare, S. and I. V. Bazarov, "Effects of surface nonuniformities on the mean transverse energy from photocathodes", Phys. Rev. Appl. **4**, 024015 (2015).

Karkare, S., S. Emamian, G. Gevorkyan, H. A. Padmore and A. Schmidt, "Physical and chemical roughness of alkali-antimonide cathodes", Proc. IPAC'18 p. 4259, URL `http://ipac2018.vrws.de/papers/thpmf080.pdf` (2018).

Krasilnikov, M., "Impact of the cathode roughness on the emittance of an electron beam", Proc. of FEL Conf. p. 583 (2006).

Martinelli, R. U., "Effects of cathode bumpiness on the spatial resolution of proximity focused image tubes", Appl. Opt. **12(8)**, 1841–1845 (1973).

Melitz, W., J. Shena, A. C. Kummela and S. Lee, "Kelvin probe force microscopy and its application", Surf. Scie. Rep. **66**, 1 (2011).

Musumeci, P., J. Giner Navarro, J. Rosenzweig, L. Cultrera, I. Bazarov, J. Maxson, S. Karkare and H. Padmore, "Advances in bright electron sources", Nucl. Instrum. Methods Phys. Res., Sect. A **907**, 209–220, URL `https://www.sciencedirect.com/science/article/pii/S0168900218303541`, advances in Instrumentation and Experimental Methods (Special Issue in Honour of Kai Siegbahn) (2018).

Parzyck, C. T., A. Galdi, J. K. Nangoi, W. J. I. DeBenedetti, J. Balajka, B. D. Faeth, H. Paik, C. Hu, T. A. Arias, M. A. Hines, D. G. Schlom, K. M. Shen and J. M. Maxson, "Single-crystal alkali antimonide photocathodes: High efficiency in

the ultrathin limit", Phys. Rev. Lett. **128**, 114801, URL `https://link.aps.org/doi/10.1103/PhysRevLett.128.114801` (2022).

Saha, P., O. Chubenko, G. S. Gevorkyan, A. Kachwala, C. J. Knill, C. Sarabia-Cardenas, E. Montgomery, S. Poddar, J. T. Paul, R. G. Hennig, H. A. Padmore and S. Karkare, "Physically and chemically smooth cesium-antimonide photocathodes on single crystal strontium titanate substrates", Appl. Phys. Lett. **120**, 19, 194102, URL `https://doi.org/10.1063/5.0088306` (2022).

Swope, W. C., H. C. Andersen, P. H. Berens and K. R. Wilson, "A computer simulation method for the calculation of equilibrium constants for the formation of physical clusters of molecules: Application to small water clusters", J. Chem. Phys. **76**, 648 (1982).

Xiang, D., W. Huang, Y. Du, L. Yan, R. Li, C. Tang and Y. Lin, "First principle measurements of thermal emittance for copper and magnesium", Proc. of PAC07 p. 1049 (2007).

Xie, J., M. Demarteau, R. Wagner, S. Schubert, M. Gaowei, K. Attenkofer, J. Walsh, J. Smedley, J. Wong, J. Feng, H. A. Padmore *et al.*, "Synchrotron x-ray study of a low roughness and high efficiency k_2cssb photocathode during film growth", J. Appl. Phys. **50**, 205303 (2017).

Zhang, Z. and C. Tang, "Analytical study on emittance growth caused by roughness of a metallic photocathode", Phys. Rev. Spec. Top. - A.B. **18**, 053401 (2015).

Chapter 3

EFFECT OF ELECTRON-ELECTRON INTERACTIONS ON THE EMISSION CHARACTERISTICS OF ULTRACOLD, NANOSCALE PHOTOCATHODES

ABSTRACT

Photoemission sources have demonstrated the potential to generate ultracold, monochromatic electrons ideal for electron microscopy. Using advanced super-resolution light microscopy techniques, it would be possible to limit the size of sources to sub-100 nm areas – potentially making them comparable in brightness to field emission tips. This chapter explores the limitations which electron-electron interactions would pose on the brightness achievable from such nanoscale, monochromatic, photoemission electron sources. Shown here are calculations of the effects of such electron-electron interactions on the transverse emittance, the energy spread and the output current from these sources. The results show an interesting regime in beam physics in which the energy spread and emittance growth are significantly mitigated due to the effects of image charge, and the primary limiter to beam brightness is the saturation current due to the electron-electron and electron-image-charge interactions.

3.1 Introduction

For the last few decades, cold field emission tips have been the brightest electron sources and have been critical in obtaining sub-atomic spatial resolutions of less than 0.05 nm from electron microscopes [Kisielowski *et al.* (2008)] in the scanning transmission mode. In a cold field emission tip, a large current of electrons is generated via field emission from a small ~ 1 n m^2 effective surface area and with a relatively large MTE and RMS total energy spread. These electrons are accelerated in an electron microscope and are collimated and often monochromatized by passing the beam through various apertures and energy filters. This monochromatization and collimation process essentially removes all but the brightest part of the electron beam emitted from field emission tips. This brightest portion of the beam is used for microscopy applications to obtain the best possible image resolution.

At the beam waist the $\langle xp_x \rangle$ correlation term in equation 1.2 is zero. For a state-of-the-art electron microscopes that can achieve a small electron spot size (and hence a small spatial resolution in the scanning transmission mode) of 0.05 nm with an convergence semi-angle of 30 mrad [Kisielowski *et al.* (2008)], the emittance of the beam is as low as ~0.5 pm-rad at the sample. The emittance obtained from a field emission tip can be several orders of magnitude larger, however after collimation in state-of-the-art electron microscopes, a current of ~ 50 pA with an energy spread of 0.8 eV can be obtained at the sample along with such a small emittance.

Recently, advanced monochromators have been employed to reduce the RMS total energy spread to as low as 10 meV at the cost of the probe current. This increases the energy resolution of Electron Energy Loss Spectroscopy (EELS) to sub-10 meV levels along with achieving a few nm spatial resolution, enabling nm-scale vibrational electron spectroscopy in electron microscopes in the scanning transmission

30

mode [Krivanek *et al.* (2014)]. However, obtaining an sufficiently sm all emittance and large enough current required for atomic-scale imaging along with a sufficiently small RMS total energy spread to enable vibrational electron spectroscopy has been impossible. The combined current reduction due to collimation and monochromatization processes leaves the probe current too small (sub fA levels) to be of much use, making it impossible to perform vibrational spectroscopy at the sub-angstrom scale in existing electron microscopes.

A potential way around this issue is to use a photoemission source with the ability to deliver pA level currents with an ultra-low emittance of the order of ~0.5 pm-rad, a small RMS total energy spread of ~ 10 meV, and a planar geometry to minimize aberrations close to the photocathode surface and the anode. Such a source would have the beam brightness comparable to that of a cold field emission gun along with a small energy spread; and although this does not exist yet, such a planar source could be developed in the future.

The smallest laser spot size on the photocathode surface is often diffraction limited to ~ 5 µm due to the largest geometrically-possible numerical aperture of the final focusing lens and the wavelength. Techniques to reduce the spot size below the this limit have been developed and implemented in super-resolution optical microscopy techniques. These include using very high numerical aperture immersion lenses or zone plate based lenses embedded into the photocathode substrate [Brunner *et al.* (2004)] or use plasmonic structures to focus light down to sub-100 nm spot sizes on the photocathode surface [Durham *et al.* (2019)]. With a combination of such techniques it is conceivable to think about photoemission spot sizes as small as to 10 nm RMS. With such small spot sizes and low sub-5 meV MTE from high QE semiconductor photocathodes, one could envision a photoemission based source that can deliver sub-pm-rad emittances along with a sub-10 meV energy spread and pA

level currents. Even though such nanoscale planar photoemission sources have not yet been realized, there is significant ongoing research in this direction and it is expected that they to become a reality in the next few years.

The advent of single-digit-meV photocathodes has made it essential to consider electron-electron interactions beyond the space charge approximation[Maxson *et al.* (2013)]. For charge densities typically found in bunched electron beam applications, the space charge approximation no longer holds true for low MTE electrons and it becomes essential to consider point-to-point electron-electron interactions. The point-to-point electron interactions lead to the disorder induced heating of the emitted electrons due to the spatially disordered nature of electron emission, increasing their MTE by a few meV depending on the charge density used and thus limiting brightness[Gordon *et al.* (2021)].

These studies regarding the limits posed to beam brightness by electron-electron interactions near the photocathode have thus far been limited to bunched electron beams with relatively large charge densities along with mm-μm sized emission areas. Furthermore these studies have never explicitly considered the effect of such interactions on the total energy spread, which is usually dominated by the RF acceleration in such applications.

In this chapter we study the effects of such coulomb interactions on electron beams emitted from the low MTE, low energy spread nanoscale photoemission sources specifically for electron microscopy applications. Our results show that the electron-electron interactions do not significantly effect the MTE or the total energy spread in certain current ranges. Furthermore, due to the low initial energy and the Poisson distribution in the time of emission of the electrons, we find that a significant fraction of the emitted electrons return back to the photocathode surface due to the repulsion from previously emitted electrons, thus limiting the total extracted beam current.

32

In section 3.2 we describe the electron-electron interaction model and the various simulation parameters used in this study. Section 3.3 shows the results of the output current, MTE and the RMS total energy spread for the simulations performed and illustrate the effects of the electron-electron interaction on the output current. In section 3.4 we discuss the brightness estimated through our computations and discuss the prospects of mitigating the electron-electron interaction effects by using a pulsed laser to emit electrons in a semi-orderly fashion in time.

3.2   Electron-electron Interaction Model and Simulation Details

In this section we provide the details of the various models we use for electron emission, image charge calculation and electron tracking. Electrons are modeled with a random initial velocity and are tracked with interactions due to an accelerating electric field and coulomb forces with other emitted electrons and image charges.

3.2.1   Electron Emission Model

In our simulations the photocathode is assumed to be in the x-y plane located at $z = 0$ and the emitted electrons are accelerated in the $+z$ direction. We assume that the x and y locations of the electrons at the time of emission are randomly distributed about the origin in a Gaussian manner with a standard deviation equal to the RMS transverse size of the source. The time of emission of each electron is chosen randomly such that the time interval between two consecutive emissions follows a Poisson distribution based on a value that is determined by our simulated beam current, which we will call the extracted current from here on. The z coordinate of all electrons at emission is z_0, a small positive value which depends on the model of the image charge used in the simulation, discussed in section 3.2.2.

The initial energy and momentum distributions are modeled to match the experi-

mentally measured distributions from a cryogenically cooled Cu(100) surface close to the photoemission threshold [Karkare *et al.* (2020)]. The emitted electron energy is chosen at random from an energy distribution given by

$$N(E)dE = Ef(E)dE, \tag{3.1}$$

where E is the kinetic energy of the emitted electron at the maximum of the potential barrier resulting from a combination of the accelerating electric field and the image charge of the emitted electron, discussed further in section 3.2.2. This distribution uses the Fermi function

$$f(E) = 1 / \left(1 - e^{\frac{E - E_{ex}}{k_B T}} \right), \tag{3.2}$$

where the excess energy $E_{ex} = \hbar\omega - \phi_{eff}$, $\hbar\omega$ is the photon energy used for photoemission and ϕ_{eff} is the effective work function after taking account the Schottky reduction due to a combined effect of the accelerating electric field and the image charge. Lastly the constant k_B indicates the Boltzmann constant and T indicates the photocathode lattice temperature.

Upon emission every electron is assigned a transverse momentum randomly chosen from a uniform distribution from 0 to $p_{\perp max} = \sqrt{2m_e E}$. The azimuthal angle that determines the direction of the transverse momentum in the x-y plane is chosen at random from a uniform distribution between 0 and 2π. More details on the tracking method can be found in section 3.2.3.

3.2.2   Model of Momentum and Energy Distributions

We use the method of images to solve the electrostatics problem of an electron leaving a metal surface, where a positive charge is introduced at an equal and opposite distance into the surface and the combined potential of the two charges is then easily calculated. Each electron produces an image charge which we include in the coulomb
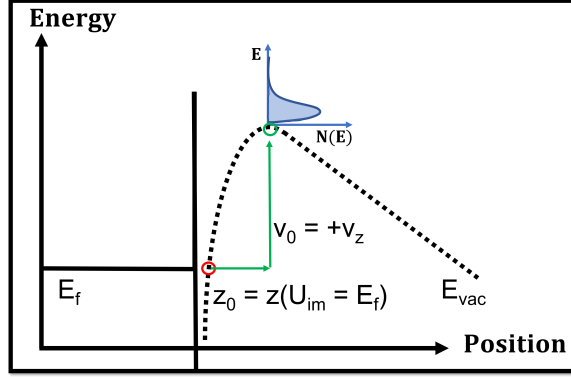
Figure 3.1: Illustration of electrons emitting from the surface to the vacuum. The work function is shown as a step potential, and the potential on the right is a combination of the image charge effect and Schottky effect. Electrons are emitted at a constant z_0 above the photocathode surface, and they are given a constant initial velocity v_0 in the direction of propagation to overcome the image charge barrier.

interaction when computing the electric potential of the system. The initial X-axis and Y-axis positions of emitted electrons are modeled by a Gaussian distribution with σ_r as the RMS beam spot size. The Z-axis position of the electrons is approximated as the location where the potential of the electric field and the image charge is equal to the Fermi energy. In figure 3.1 we show a potential map of electrons after leaving the surface.

If electrons were generated at the photocathode surface where $z_0 = 0$, then their potential due to the image charge would immediately force them back to the photocathode surface. Instead of this, the Z-axis initial position of electrons is approximated as the location where the potential of the electric field and the image charge is equal to the Fermi energy,

$$z_0 = \frac{-\phi + \sqrt{\phi^2 + \frac{E|e^-|}{4\pi}}}{2E}. \tag{3.3}$$

In this equation ϕ is the work function of the material, E is the applied electric field, and $|e^-|$ is the electron charge. The initial velocity of electrons is dictated entirely by the energy requirements of electrons. Generated electrons fall within a uniform range of kinetic energy set by an inputted value. The kinetic energy can be thought of as

having two distinct aspects, the variable aspect with direction distributed uniformly along all three axes, and the constant aspect, v_0, directed entirely into the Z axis and is equal to the minimum energy required to overcome the attraction of the image charge. When combined, these aspects ensure that all electrons are able to travel along the Z axis while also being within the desired range of kinetic energy and the desired direction distribution of velocity. We have verified that all emitted electrons fall within the correct ranges and have the necessary energy to overcome the attraction of the image charge.

3.2.3 Electron Tracking

Electrons trajectories over arbitrarily small time-steps are computed using the symplectic Velocity Verlet algorithm [Swope *et al.* (1982); Gevorkyan *et al.* (2018)]. The acceleration is found for each electron at each time-step using the electric potential due to the applied electric field, each individual electron, and their respective image charges. A small time-step is required for reasonable accuracy because we are using a 2$^{\text{nd}}$ order symplectic algorithm.

For computations with this algorithm, insufficiently small time-steps typically result in a variance of computed velocities which simply increases the energy spread. However, in our case it results in a loss of electrons due to the inclusion of image charge. There is a steep electric potential in the region closest to the photocathode surface as seen in figure 3 .1. Tracking electrons with insufficient time-steps causes electrons to accelerate back to the surface due to the short spatial scales and small energy spreads of the simulated electrons. The problem is made even more complicated with the inclusion of more than one electron at any time. With the computational resources available to us, we generated and tracked electrons using a sufficiently small time-step of 10^{-20} seconds; with this time-step less than 2% of electrons are lost due

36

to kinematics inaccuracies in the computation. Higher order symplectic integrators could be used for faster computations in the future [Ruth (1983); Forest and Ruth (1990); Forest (2006); Yoshida (1990); Candy and Rozmus (1991)], however implementing these for a varying electric potential multi-body problem is nontrivial.

The extracted current follows a Poisson distribution. The "output" current is the fraction of the extracted current that has reached a z-axis position of $1.0\,\mu m$ above the photocathode and has below a 1.0 meV electric potential with the rest of the electrons and image charges. A portion of the extracted current is not emitted when electrons which are lost because they have returned to the surface, $z = 0$. The simulation continuously computes electron emissions and trajectories until a few hundred electrons have been counted as "output" to provide sufficient statistics for analysis.

3.3   Computational Results and Explanation

We used this computation model to evaluate electron beams with extracted currents between 0.1 nA and 100 nA, with beam spot sizes of 10 nm, 50 nm, and 100 nm, all computed with an applied an electric field of 1.0 M V/m. An initial expectation of this simulation would be that the MTE and the RMS total energy spread would limit the maximum brightness as the current approaches saturation, and the energy variation would increase as the spot size decreases. Our computation suggests that this is not the case, and that the current is the largest limiter in beam brightness.

3.3.1   Current Saturation Due to Electric Potential Barrier Changes

We evaluate a simpler two electron model analytically to estimate what we expect to see as the current saturation. When there is only a single electron in the system,
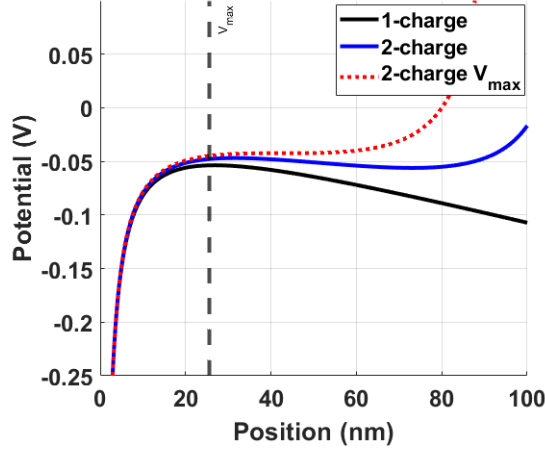
Figure 3.2: We plot the potential barriers shown in 3.4 and 3.6 for various distances d. A local maxima for the single electron case can be solved in 3.5, marked by a vertical line. Similar local maxima can be found on the two electron case up until the second electron is brought a distance d_{min} to the surface; that is the distance where the local maxima disappears.

we can write the electric potential barrier for that electron as,

$$V_{1_{barrier}} = |e^-|E_0 - \frac{k_e|e^-|}{2z'}, \tag{3.4}$$

where $|e^-|$ is the electron charge, E_0 is the applied electric field, k_e is the Coulomb constant, and $2z'$ is the distance between the electron and its image charge. The peak of this barrier can be solved directly,

$$z_{1_{peak}} = \sqrt{\frac{k_e|e^-|}{2E_0}}. \tag{3.5}$$

For the sake of simplicity, we consider the additional potential of a stationary second electron a close distance d away from the surface,

$$V_{2_{barrier}} = |e^-|E_0 + \frac{k_e|e^-|}{d-z'} - \frac{k_e|e^-|}{d+z'} - \frac{k_e|e^-|}{2z'}. \tag{3.6}$$

The local peak of the electric potential barrier $V_{2_{peak}}$ for the emitted electron increases according to the distance d. In figure 3.2 we plot the electric potential from equations 3.4 and 3.6.
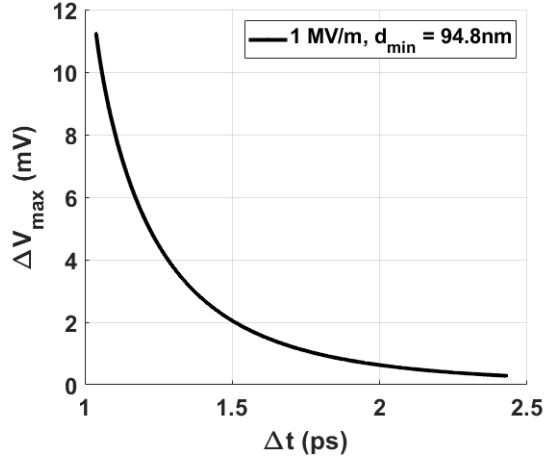
Figure 3.3: Change in the peak electric potential barrier where the vertical axis $\Delta V_{peak} = V_{2_{peak}} - V_{1_{peak}}$ is plotted versus the emission interval δt of a second electron placed along the direction of the beam. The potential barrier increases rapidly as the emission interval approaches the saturation limit.

At some close distance d the local peak disappears entirely, meaning that an electron that is emitted would return to the surface. To detail the growth of the potential barrier's local maxima in the two electron case, we plot in figure 3.3 the change in the potential barrier versus the distance d where the second electron is placed.

Given a finite energy spread, the plot indicates that there is a temporal spacing cut-off where the emitted electron would not have enough energy to overcome the potential barrier and therefore return to the surface after emission. This implies there is a saturation current,

$$I_{sat} = \left(\frac{2m_e d_{\min}}{|e^-|^3 E_0}\right)^{-1/2}, \tag{3.7}$$

where I_{sat} is the saturation current, m_e is the rest mass of the electron, and $d_{\min}$ is the closest spacing between subsequent electrons due to an increased peak potential barrier. For a 1.0 MV/m applied electric field, we predict the saturation current to be $0.154\,\mu A$.

In figure 3.4 we plot the output current for the three spot sizes as a function of

39
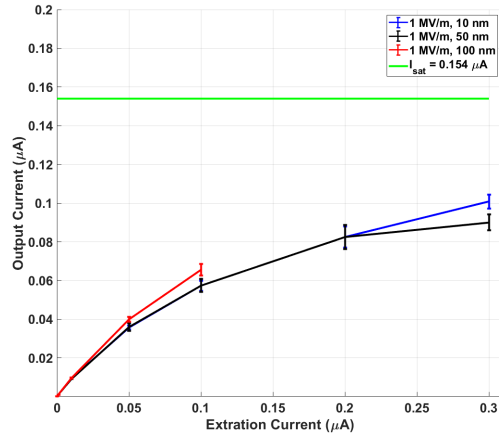
Figure 3.4: These plots show the change in the output current emitted versus the extracted currents ranging from 0.1 nA to 0.3 µA. The blue, black, and red curves represent the 10 nm, 50 nm, and 100 nm beam spot sizes respectively. The green line is the calculated saturation limit for the 1.0 MV/m electric field.

the extracted current. The output current tends toward the estimated saturation limit as explained in our simple two electron case, making it an effective first guess. The number of interacting electrons in the system increases as the emitted current increases, making our saturated current estimate slightly larger than what was computed. A more accurate estimate would not be possible to solve analytically due to the increasing number of electron interactions.

3.3.2 MTE and RMS Total Energies in the Nanoscale Emission Regime

There is an initial assumption that the MTE and RMS total energy spread would increase significantly in the nanoscale emission regime due to the closer electron spacing. We show in figure 3 .5 t he M TE a nd R MS t otal e nergy s preads o f electrons emitted for our inputs. The results show MTE values remain quite low between 4 meV and increase up to 14 meV for the highest extracted currents. The RMS total energy spreads remain between 5 meV to 25 meV for each spot size even at higher output currents. Both of these quantities remain significantly low even for the small-
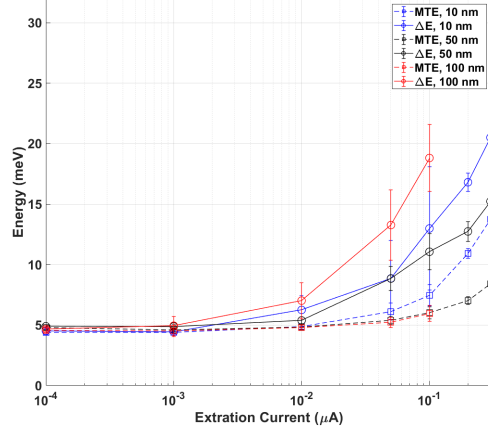
Figure 3.5: Plot of MTE (dashed lines) and RMS total energy spread (solid lines) versus the extracted current. The colored lines distinguish the RMS laser spot sizes of 10 nm (blue), 50 nm (black), and 100 nm (red). Both increase as the extracted current approaches the saturation limit.

est spot sizes, and remain low until the extracted current approaches the saturation limit as described in section 3.3.1; this result is opposite to initial expectations for photoemission in this regime.

To illustrate an explanation, we show a simplified force diagram of the interaction of each electron with the field, a second electron, and their respective image charges in figure 3.6.

The transverse forces experienced by the electrons are

$$F_\perp = k_e |e^-|^2 \left(\frac{r}{(r^2 + (z-d)^2)^{3/2}} - \frac{r}{(r^2 + (z+d)^2)^{3/2}} \right), \tag{3.8}$$

where z and d are the longitudinal distances between the emitted electron to the photocathode and second electron to the photocathode respectively, and r is the transverse distance between the respective electrons. The first term in the force is the transverse push of the second electron, and the second term is the transverse pull of the second electron's image charge.

The mitigation of MTE is a result of the image charge interaction at the close surface distances [Gordon *et al.* (2021)]. At the highest extracted currents the MTE
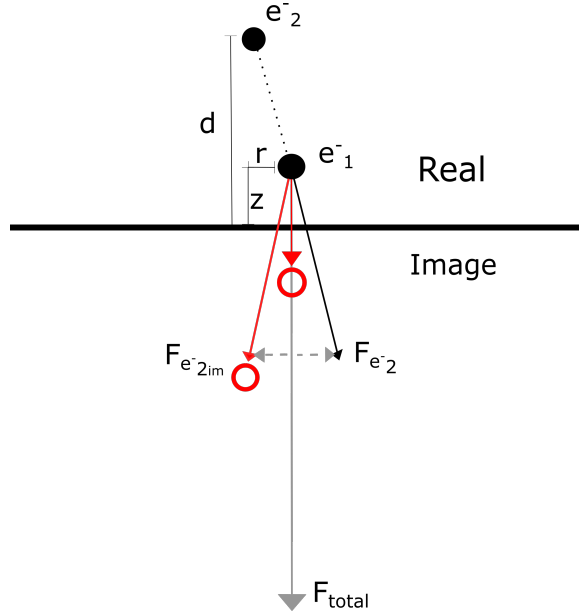
Figure 3.6: Force diagram of two electrons (black) labeled as e_1^- and e_2^- and their respective image charges (shown in red). This illustration shows the forces experienced by the electron e_1^-. The horizontal components of the forces due to the 2nd electron ($F_{e_2^-}$) and its image charge ($F_{e_{2_{im}}^-}$) approximately cancel at very close distances. The three vertical forces due to the self-image, the second charge, and the second charge's image all sum together, and the resultant force of the system is (F_{total}).

grows because we are attempting to operate near or above the saturation limit, as discussed in section 3.3.1, and there are significantly more interactions at a smaller area. Even so, the MTE remains quite low at these nanoscale spot sizes.

The RMS total energy spreads, according to our force diagram in figure 3.6, should have increased significantly with the inclusion of image charge due to the longitudinal forces between image charge and real charges adding together. Although the RMS total energy spreads do increase more than the MTE, it still remains significantly lower than initial expectations for such a nanoscale source given that the image charge adds constructively with the real charge longitudinally.

To explain this effect, in figure 3.7 we show cross sections of a 3D scatter plot for each electron emission, plotting the total energy verses the emission time interval versus the radial distances between subsequent electrons.
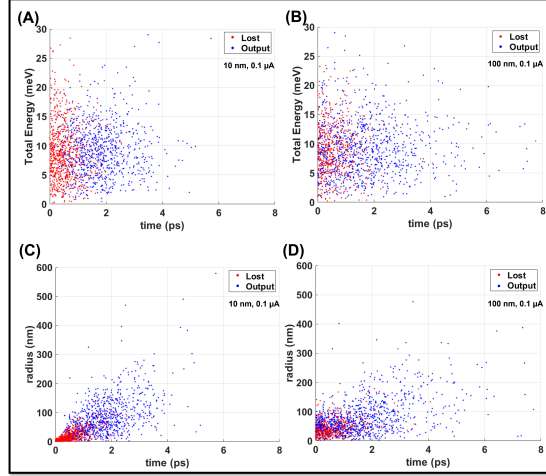
Figure 3.7: 2D cross sections of a 3D scatter plot, plotting total energy versus emission time interval after previous emission versus radial distances between subsequent electrons for an extracted current of 0.1 µA. The blue and red data points distinguish between electrons which were output and electrons which returned to the photocathode surface respectively. Plots (3.7a) and (3.7b) show the total energy vs emission time interval for the simulation of 10 nm spot size and 100 nm spot size respectively. Plots (3.7c) and (3.7d) show the radial distances between subsequent electrons vs emission time interval for the same. The data indicates that electron emissions are both related to the emission time interval and the radial separations.

The electrons which return to the photocathode surface after emission, denoted in red, condense within a specific emission interval as the current approaches the saturation limit, validating our explanation in section 3.3.1. The longitudinal force of subsequent electrons increases with smaller electron spacing; the smallest beam spot size actually has less output current (8% less in this case) due to electrons returning to the surface which accounts for the smaller total RMS energy spread. The lower energy electrons emitted at closer radial distances are more likely to be pushed back into the surface at higher extracted currents. This effectively ”cleans” the RMS total energy spread in the smaller spot sizes. The electrons emitted at larger radial distances interact less longitudinally in the first place, meaning less increase in total energy spread.
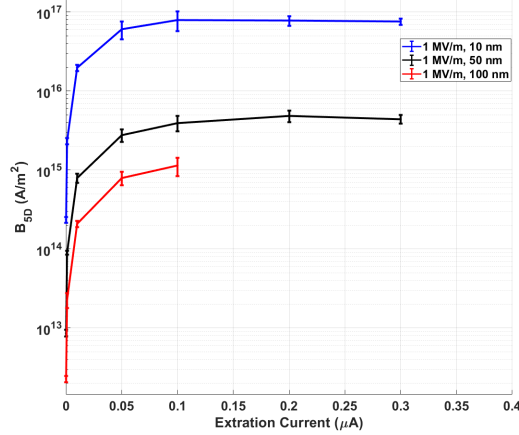
Figure 3.8: Plot of B_{5D} for varying laser spot sizes and extracted currents. Brightness goes up to the $10^{15}[a/m^2]$ range, which is two orders of magnitude higher than the $6 \times 10^{13}[A/m^2]$ cold field emission tips used in modern electron microscopes. The brightness eventually begins to decrease due to diminishing returns from the output current and increases in the MTE at higher extracted currents.

3.4   Conclusion and Future Work

The 5D beam brightness of the nanoscale photocathode that we've simulated thus far can be quantified by using equations 1.1 and 1.4,

$$B_{5D} = \frac{2I(m_0 c^2)}{\pi^2 \mathrm{MTE} \sigma_i^2}. \tag{3.9}$$

The constant $m_0 c^2$ indicates the electron's rest mass energy, the variable σ_i indicates the laser spot size, the variable I indicates the output current. A plot of the 5D brightness using the equation 3.9 is shown in figure 3.8.

The 5D beam brightness of such a photocathode would reach the $10^{15}[A/m^2]$ range or higher. The best electron microscope use cold field e mission g uns, which have a brightness up to 6×10^{13} $[A/m^2]$ [Spence and Howells (2002)]. Those electron guns produce electron beams with RMS total energy spread in the 300 meV range and require the use of monochromators to reduce the energy spread, whereas this photoemission source would have non-monochromated RMS total energy spreads in the 10's of meV. Further investigations will be done for higher accelerating gradients

44

and the dependence on radius for these ultra-low emittance photocathodes.

The benefit of this source over traditionally used sources is significantly smaller transverse and longitudinal energy spreads. The primary concern is whether it is possible to extract the necessary current for various electron beam applications. To extract $0.1\,\mu A$ of current from a photocathode with 1% QE, we would need $50\,\mu W$ squeezed into a $20\,nm$ laser beam spot size. This would be a laser irradiance of $1\,GW/cm^2$

A pulsed laser could be used to limit electron-electron interaction effects in higher current applications by emitting electrons in a semi-orderly fashion. For a 1.0 MV/m electric field, an output current of $80\,nA$ suggests that a 500 GHz repetition rate pulsed laser would help further reduce the increased energy spread of the beam and increase the output current closer toward the saturation limit.

3.5   Acknowledgements

REFERENCES

Brunner, R., M. Burkhardt, A. Pesch, O. Sandfuchs, M. Ferstl, S. Hohng and J. O. White, "Diffraction-based solid immersion lens", JOSA A **21**, 7, 1186–1191 (2004).

Candy, J. and W. Rozmus, "A symplectic integration algorithm for separable hamiltonian functions", Journal of Computational Physics **92**, 1, 230–256 (1991).

Durham, D. B., F. Riminucci, F. Ciabattini, A. Mostacci, A. M. Minor, S. Cabrini

and D. Filippetto, "Plasmonic lenses for tunable ultrafast electron emitters at the nanoscale", Phys. Rev. Appl. **12**, 5, 054057 (2019).

Forest, E., "Geometric integration for particle accelerators", Journal of Physics A: Mathematical and General **39**, 19, 5321 (2006).

Forest, E. and R. D. Ruth, "Fourth-order symplectic integration", Physica D: Nonlinear Phenomena **43**, 1, 105–117 (1990).

Gevorkyan, G. S., S. Karkare, S. Emamian, I. V. Bazarov and H. A. Padmore, "Effects of physical and chemical surface roughness on the brightness of electron beams from photocathodes", Phys. Rev. Accel. Beams **21**, 093401, URL `https://link.aps.org/doi/10.1103/PhysRevAccelBeams.21.093401` (2018).

Gordon, M., S. Van Der Geer, J. Maxson and Y.-K. Kim, "Point-to-point coulomb effects in high brightness photoelectron beam lines for ultrafast electron diffraction", Physical Review Accelerators and Beams **24**, 8, 084202 (2021).

Karkare, S., G. Adhikari, W. A. Schroeder, J. K. Nangoi, T. Arias, J. Maxson and H. Padmore, "Ultracold electrons via near-threshold photoemission from single-crystal cu(100)", Phys. Rev. Lett. **125**, 054801, URL `https://link.aps.org/doi/10.1103/PhysRevLett.125.054801` (2020).

Kisielowski, C., B. Freitag, M. Bischoff, H. Van Lin, S. Lazar, G. Knippels, P. Tiemeijer, M. van der Stam, S. von Harrach, M. Stekelenburg *et al.*, "Detection of single atoms and buried defects in three dimensions by aberration-corrected electron microscope with 0.5-å information limit", Microscopy and Microanalysis **14**, 5, 469–477 (2008).

Krivanek, O. L., T. C. Lovejoy, N. Dellby, T. Aoki, R. Carpenter, P. Rez, E. Soignard,

J. Zhu, P. E. Batson, M. J. Lagos *et al.*, "Vibrational spectroscopy in the electron microscope", Nature **514**, 7521, 209–212 (2014).

Maxson, J., I. Bazarov, W. Wan, H. Padmore and C. Coleman-Smith, "Fundamental photoemission brightness limit from disorder induced heating", New Journal of Physics **15**, 10, 103024 (2013).

Ruth, R. D., "A canonical integration technique", IEEE Trans. Nucl. Sci. **30**, CERN-LEP-TH-83-14, 2669–2671 (1983).

Spence, J. and M. Howells, "Synchrotron soft x-ray and field-emission electron sources: a comparison", Ultramicroscopy **93**, 3, 213–222, URL `https://www.sciencedirect.com/science/article/pii/S0304399102002784`, special issue in Honour of Peter W. Hawkes on the Occasion of his 65th Birthday, in Recognition of his Contributions to Electron Optics and Electron Microscopy (2002).

Swope, W. C., H. C. Andersen, P. H. Berens and K. R. Wilson, "A computer simulation method for the calculation of equilibrium constants for the formation of physical clusters of molecules: Application to small water clusters", The Journal of chemical physics **76**, 1, 637–649 (1982).

Yoshida, H., "Construction of higher order symplectic integrators", Physics letters A **150**, 5-7, 262–268 (1990).

Chapter 4

A CRYOGENICALLY COOLED 200 KV DC PHOTOEMISSION ELECTRON GUN FOR ULTRALOW EMITTANCE PHOTOCATHODES

ABSTRACT

Novel photocathode materials like ordered surfaces of single crystal metals, epitaxially grown high quantum efficiency thin films, and topologically non-trivial materials with Dirac cones show great promise for generating brighter electron beams for various accelerator and ultrafast electron scattering applications. Despite several advanced photocathodes having been identified with the potential to produce brighter electron beams, none of them have been tested in electron guns to extract electron beams due to technical and logistical challenges. Presented in this chapter is the design and commissioning of a cryocooled 200 kV DC electron gun which is capable of testing a wide variety of novel photocathode materials over a broad range of temperatures from 298 K to 35 K for bright electron beam generation. This gun is designed to enable easy transfer of the photocathode to various standard ultra-high-vacuum surface diagnostics and preparation techniques allowing a full characterization of the dependence of beam brightness on the photocathode material and surface properties. This chapter details the development of such a high-voltage-high-gradient gun using materials and equipment that are easily available in any standard university lab making development of such 200 kV electron guns more accessible.

4.1   Introduction

As described in chapter 2, low MTE photocathodes are limited by the effects of surface non-uniformities such as physical roughness and work function variation, making it critical to use single-crystalline, atomically ordered photocathode surfaces for the smallest possible MTE. In chapter 3 we showed the potential of such photocathodes if operated in the optimal photoemission regime with nanoscale laser spot sizes. Many advanced photocathodes have been identified that show promise of higher beam brightness but have never been tested in electron guns with large accelerating gradients and capable of generating high energy electron beams. This is primarily due to the design incompatibility of existing electron guns with the tools necessary to prepare the vacuum sensitive surfaces of such photocathode technologies and other logistical issues.

Most RF guns use the backside plate of the RF cavity, a piece of machined copper, as their electron source. A new style of retractable photocathode plugs originally designed at the National Institute for Nuclear Physics (INFN), Italy, are becoming more popular in RF guns [Sannibale *et al.* (2012); Rosenzweig *et al.* (2018)] because they allow for the growth and use of thin films vacuum sensitive photocathodes like alkali-antimonides and Cs_2Te. However, the polycrystalline nature of the machined metal plug allows for the growth of only rough polycrystalline films of the high QE photocathodes[Alesini *et al.* (2015)]. The INFN pucks do not have a clear way of mounting a single-crystal surfaces, and any mounted surface would ruin the electrostatic configuration due to sharp edges introduced by traditional substrate mounting methods.

Some RF guns like the L-band gun at the Argonne Wakefield Accelerator facility [Conde *et al.* (2017)] and several DC guns used for polarized electron generation

[Siggins *et al.* (2001)] and extremely high currents [Dunham *et al.* (2013)] can use substrates mounted to the photocathode plug, however, they require substrates of non-standard dimensions making it challenging to acquire, use and test a wide variety of non-traditional materials as photocathodes or substrates. Most of these guns do not have the appropriate UHV surface preparation and characterization tools required for the advanced photocathodes. Also, none of these guns allow for cooling the photocathode to cryogenic temperatures or have tunable wavelength lasers easily available which may be required to test the production of the brightest beams. Furthermore, many of these guns provide electrons to operating facilities and testing a wide variety of photocathode materials becomes a logistical challenge.

In order to address the need of a photocathode test bed for such advanced, low MTE photocathodes, we have designed and built a 200 kV cryocooled DC electron gun [Gevorkyan *et al.* (2019, 2022)] at Arizona State University (ASU). In this chapter we present the design, construction, and commissioning of the ASU 200 kV DC cryocooled electron gun. This gun uses the Omicron flag style sample holder [Scienta Omicron GmbH (2023)] as the photocathode. Such a sample holder is compatible with several commercial surface science instruments and can hold the 10 mm X 10 mm substrates that are most commonly available. Although this gun has been primarily developed for photocathode studies, it can also be used as a source of electrons for UED applications. We have also designed the gun to use a continuous flow liquid Helium (LHe) cryostat to minimize vibrations during cold operation. Due to potentially low MTE and vibration free cryogenic operation, in principle, it can outperform existing UED setups [Filippetto and Qian (2016); Li *et al.* (2022); Gordon *et al.* (2022)] in terms of the resolution and signal-to-noise ratio.

Furthermore, most high-voltage-high-gradient DC guns used as electron sources have been developed at large laboratories with specialized equipment for cleaning and

polishing the electrodes. The ASU gun presented here has been developed using only equipment easily available at a small university scale lab making the development of such guns more accessible. In section 4.2, we present the mechanical, vacuum, electrostatic high voltage and cryogenic design of this gun. In section 4.3 we give details of the assembly process and demonstrate the cryogenic and high voltage performance of the gun and show its commissioning process to high voltage. Finally in section 4.4 we discuss the future plans for operation of this gun.

4.2   Electron Gun Design

4.2.1   Mechanical and Vacuum Design

The ASU cryogun is an inverted geometry electron gun [Hernandez-Garcia *et al.* (2016, 2019); Adderley *et al.* (2010); Nagai *et al.* (2010); Maxson *et al.* (2014)]. The design was based on the Cornell 200 kV DC cryocooled electron gun [Lee *et al.* (2018)] and has modifications to incorporate the following features:

(a) Flexibility to implement a variety of photocathodes.

(b) Capability to transfer photocathodes easily into and from standard UHV surface preparation and characterization tools.

(c) Thermal radiation shield to minimize photocathode temperature for a given cooling power.

(d) Use of continuous a flow cryostat to minimize vibrations during cryogenic operations.

(e) Multiple laser beam input angles to test photocathode performance as a function of the angle of incidence.

To have these features, we modified t he s hapes o f t he e lectrodes a nd t he anode, used a larger vacuum chamber, used a custom photocathode puck design, and changed

51

the design of the core. A cross section of the ASU electron gun is shown in figure 4.1 to illustrate the design with various key components labeled. The photocathode is
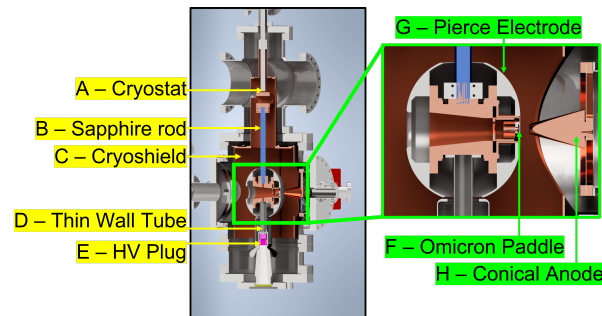
Figure 4.1: Cross-section of the ASU electron gun. At the top of the gun is a continuous flow cryostat which cools the electrodes and photocathode. The cryostat cold head is connected to the core through a flexible copper strap and sapphire rod in order to maximize the thermal conductance while staying electrically insulated [Dobrovinskaya *et al.* (2009)]. The cryostat also cools a copper cryogenic shield which reduces black-body radiation to the cold internals of the gun and helps obtain lower temperatures at the photocathode. We use a stainless-steel thin wall tube with patterned holes connected directly to the hv plug; this tube thermally insulates the core from the room temperature hv plug while still maintaining electrical conductivity. A closer look into the heart of the gun, outlined in green, shows that we use a custom puck to insert an Omicron paddle mounted photocathode covered by a spherical electrode with Pierce geometry to cover any sharp edges from being exposed to the high gradient fields. The anode is conical in shape to both maximize the accelerating gradient at the photocathode surface and also to allow for multiple laser beam input angles.

placed on a puck which can be inserted into a copper block (the core) in the electron gun. The core is enclosed by a pair of well polished, hemispherical electrodes made from 316 stainless-steel (316 SS). These form a spherical electrode shell to ensure all sharp corners of the core are electrically shielded and are not exposed to large electric fields. The back part of the shell has an opening where we insert the puck holding the photocathode into the core. The front part of the shell facing the anode has a Pierce geometry [Stoffel and Johnson (1985)], exposing only the flat portion of the the photocathode to the high electric fields in the photocathode-anode gap. This geometry is necessary to cover the sharp edges of our photocathode substrate and mount as we discuss in the next paragraph.

The puck nests within an RF conducting spring [Stäubli International AG (2019)] placed inside the core to keep it in place and provide a good thermal and electrical contact. The transfer arm has a bayonet which can lock into the back of the puck to move it into and out of the core. This puck has a saddle in which the Omicron flag-style sample holder [Karkare *et al.* (2019)] is inserted. photocathode substrates of any size larger than 9 mm diameter and smaller than 14 mm × 14 mm square can be mounted to this flag-style holder using tantalum strips spot welded to the holder. This holder is compatible with the other commercial surface science tools also available in the lab allowing us to easily use single crystal or epitaxially grown photocathodes inside the electron gun while providing the flexibility needed to study a wide range of materials.

The shell and the core are connected to the high voltage UHV feed-through via a long thin tube made from 316 SS. This tube mechanically supports the photocathode electrode assembly, provides the HV connection and minimizes heat conduction from the HV feed-through. This tube is enclosed with a larger, well polished, cylindrical, 316 SS outer tube to shield it from the large electric fields. The larger outer tube is connected to the HV feed-through and does not come in direct contact with the cold photocathode assembly limiting the conductive heat loss only through the thin inner tube. The HV feed-through is isolated from the grounded chamber walls using a ceramic insulator shaped to allow insertion for the R-28 HV plug on the HV cable connecting the high voltage power supply (HVPS) to the gun outside of vacuum.

The top of the core is connected to a continuous flow LHe cryostat through a thermally conducting, but electrically insulating sapphire rod. The sapphire rod is connected to the cryostat using a flexible copper strap. Our electron gun design has the HV plug on the bottom and the cryogenic cooling mechanism above on the top to accommodate the long insertion length of the cryogenic LHe transfer line into the

cryostat. This allows us to keep the photocathode at a comfortable height to transfer it into and out of the gun in UHV. We have added a cryogenic shield which covers the cold photocathode/shell of the gun. This intermediate temperature barrier shields the cold parts from the chamber's black-body radiation and helps the photocathode reach lower temperatures. The cryogenic shield is cooled by the exhaust of the cryostat.

The gun chamber and the electrodes are designed to give us additional laser beam input angles. In figure 4.2 we show a horizontal cross section of the gun to illustrate the possible laser beam input angles and also how pumping to UHV was achieved.
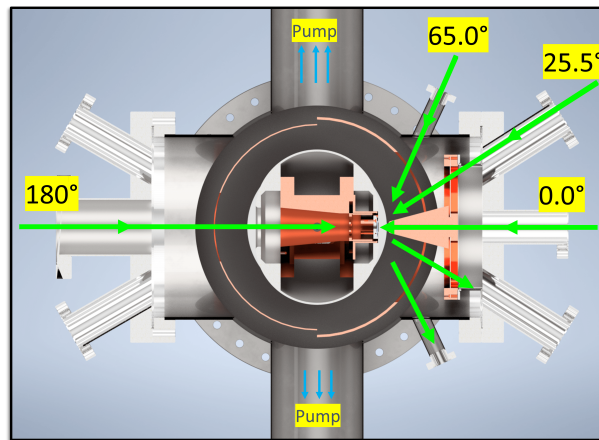
Figure 4.2: The conical anode shape allows for four laser beam input angles, one directly through the anode hole, one through the backside of the photocathode for photoemission in the transmission mode, one at 25.5° and another at 65.0° both with respect to the photocathode surface normal. We also display the cryogenic shield enclosing the electron gun electrodes which consists of two cylindrical copper sheets with different r adii. This l eaves a g ap w hich i mproves t he g as conductance by providing a path to two symmetric SAES NEG/Ion combo pumps connected on the electron gun chamber.

The two laser beam input angles at the front of the gun are 25.5° and 65.0° with respect to the photocathode surface normal. The beam can also be incident on the photocathode at near normal angle by reflecting it off a mirror which can be inserted in the electron beamline. A laser path through the backside of the photocathode exists to allow the possibility of using photocathodes in the transmission mode. The QE of certain materials, especially metal surfaces, varies with photoemission angles

and light polarization [Karkare *et al.* (2017)]. These various openings can allow for the study of the photocathode performance at different angles of incidence.

Figure 4.2 also shows that the cryogenic shield covering the cryogenically cooled interior is made of two parts of different radii. With this design we require an opening near the pump locations to give us higher gas conductance from the photocathode surface to the pumps while still shielding the photocathode from room temperature radiation heating. The vacuum requirement is then achieved by using two 2000 L/s SAES NEXTorr D2000 [Manini and Maccallini (2017); SAES Getters S.p.A. (2022)] NEG/Ion combo pumps placed symmetrically on both sides of the chamber facing the spherical electrode shell. The chamber reaches pressures well below 10^{-10} torr, a typical range for electron gun operation.

4.2.2   High Voltage Design

The ASU electron gun uses a larger vacuum chamber with a 13.25" ConFlat [Kurt J. Lesker Company (2022)] (CF) flange as opposed to the chamber with a 10" CF flange as used for the Cornell gun [Lee *et al.* (2018)]. The larger chamber was chosen to obtain our desired electrostatic configuration - 10 MV/m at the photocathode - after adding the additional element of a cryogenic shield. The cryogenic shield is grounded and kept at the same distance away from the negatively biased shell as the chamber walls of the Cornell gun. This requires the ASU gun to use a larger vacuum chamber to enclose the cryogenic shield.

The electrostatic fields of the ASU electron gun have been computed using Poisson Superfish [Halbach (1976)]. Figure 4.3 displays the design and geometry of our electrode and the equipotential field lines formed between the photocathode and anode when at high voltage. The puck sits behind the spherical electrode shell which has been modified in shape from what was used in the Cornell gun to cover the protruding

saddle holding the sample holder and prevent sharp corners from being exposed to the large electric field between the photocathode and anode. A 9.0 mm diameter circular section of the photocathode surface is exposed to the large electric fields between the photocathode and anode. This limits the smallest size wafer that can be used in the gun without exposing the sharp edges to large electric fields.
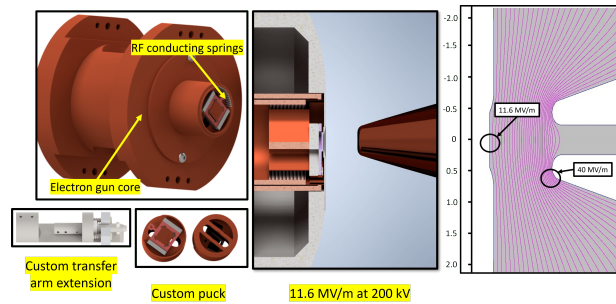
Figure 4.3: The electron gun core has been modified to accommodate a custom-made photocathode puck. We mount our custom-made puck within an RF conducting spring inlaid within the gun's core. The puck contains a Ferrovac saddle where we insert an Omicron flag-style paddle photocathode holder. Our custom transfer arm extension fits to the back slot of the puck, allowing us to easily insert and remove the puck from the core. When the photocathode voltage is set to -200 kV, the electric fields at the photocathode surface reach 11.6 MV/m. The fields near the grounded anode reach high as 40 MV/m.

The anode is bolted to the front flange on the vacuum side of the electron gun chamber. Increasing the chamber size to implement a grounded cryogenic shield has increased the distance between the photocathode and anode. The anode was modified from being a flat grid plate with a hole as in the Cornell DC gun case, to being conical in shape, allowing the anode nose to sit as close as possible to the photocathode surface to form high accelerating gradients while still providing a path for the laser beam at the various angles.

The gap between the photocathode and anode is 1.17 cm, and the fields produced at the center of the photocathode surface reach 11.6 MV/m when the gun is operated at -200 kV due to the shape of the anode. Due to the curvature of the anode nose, the fields there are as high as 40 MV/m at -200 kV. The photocathode field is typically

limited to the 10 MV/m range due to field emission, however the anode field can be significantly higher because the emission of ions from the anode requires significantly larger fields [Miller and Kenik (2004)]. The anode field of 40 MV/m is about a factor of three higher than what is used in many DC guns, including the Cornell Cryogun. However the anode field of 40 MV/m was not a limitation in achieving the required gun voltage as shown in section 4.3.

The Pierce geometry at the photocathode cause focusing electric fields whereas the anode hole causes electric field lines that tend to defocus the emitted electron beam. The radial components of these fields are linear with the radius to first order, and these cause linear lensing of the electron beam. Linear lensing effects do not affect the emittance, however higher order nonlinearities in the field do cause emittance degradation. To determine the region where these focusing/defocusing field lines do not degrade the emittance, we conducted a beam size scan using GPT [van der Geer and de Loos (1997)] to simulate the motion of emitted electrons until they pass through the anode. The simulation assumes no space charge effects. Figure 4.4 displays the result of this computation.

For 30 keV electron beams, a laser spot smaller than 800 μm at the photocathode center yields a change in beam emittance of below 0.2%. For beams at 200 keV, a laser spot smaller than 600 μm at the photocathode center is needed to yield a similar change in beam emittance. This shows that the non-linear effect due to the photocathode/anode focusing are negligible so long as the emission area is restricted to within the central 500 um - 1000 um region depending on the gun voltage and photocathode MTE.
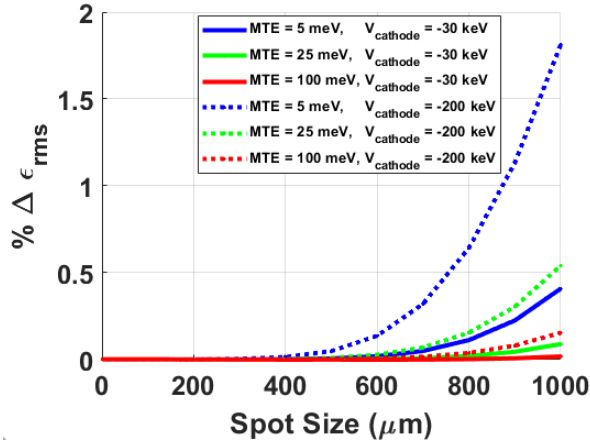
Figure 4.4: A GPT simulation was used to demonstrate the effect of the gradient non-linearities from 30 keV (solid) to 200 keV (dashed). The electron beam MTE and spot sizes are varied, and electrons were tracked from the photocathode through the anode. This computation shows that the emission area of the gun should be restricted to a laser beam radius of 800 µm and below in order to avoid the non-linear effects of the field. This simulation assumes no space charge.

4.2.3   Cryogenic Design

Cryogenic Cooling Systems and Design

Cooling the photocathode to cryogenic temperatures is a major design feature of the Cornell Cryogun, and the ASU electron gun uses the same heat extraction design within the gun but uses a different cryogenic cooling system with a cryogenic shield. The Cornell Cryogun uses a closed-cycle cryostat which introduces vibrations that can be detrimental to the emittance at the nanometer-radian scale. We addressed this issue on the ASU gun by using a continuous flow cryostat. The exhaust of the cryostat is used to cool the cryogenic shield and is then captured and pumped into a helium liquifier for reliquification. We use the Cryomech Helium Liquefier Plant which can generate up to 24 liters per day of LHe from He gas. This limits the maximum flow rate of LHe through the cryostat to 24 liters per day for continuous use without loss of He gas.

The Cryomech Helium Liquefier Plant used in our lab refrigerates and supplies a

continuous flow of LHe to the cryostat of the gun. The system is able to replenish 24 liters per day, making that our maximum stable flow for indefinitely long cooling. The LHe flows through the cryostat connected to the gun's flexible copper strap, evaporating and removing heat from the gun. The helium gas is recirculated back into the liquefier plant through the use of a scroll pump. When the gas pressure in the 150 L dewar of the plant increases beyond 10 PSI, a relief valve releases the excess gas out of the system resulting in a loss of helium. Helium is replenished by attaching a standard gas container of 99.999% pure LHe and pumping it into plant. So long as the flow rate of liquid helium is kept below the maximum 24 liters per day liquification capacity, the pressure in the dewar does not increase and no helium is lost.

In order to maximize the heat extraction between the cryostat and the core, the ASU electron gun uses a P5-502 CuTS copper strap [Technology Applications, Inc. (2022)] connected to the cryostat to allow for flexibility while maintaining maximum thermal conduction to extract heat from the electrode and photocathode. We connect a 21.0 mm diameter, 25.4 cm long sapphire rod from Precision Sapphire Technologies [Precision Sapphire Technologies, Ltd. (2022)] between the copper strap and electron gun core to extract heat from the photocathode and cool it to cryogenic temperatures while isolating the core and the shells electrically from the copper strap. We place a 0.127 mm thick layer of indium foil[John and Hilliard (1963)] in between joints where two materials connect to improve the thermal conduction.

In order to minimize the heat conduction from the cold core to the room temperature HV feed-through, this gun uses a thin stainless steel tube with patterned holes between the core and the high voltage plug. The patterned holes remove nearly half of the mass of the tube, reducing the thermal conductivity by half while still maintaining its structural stability. The thickness of the tube is 0.5 mm and the length is

10.16 cm. The ASU gun uses a polished copper shield between the vacuum chamber walls and the cold electrode shells in order to minimize the radiation heating. There are holes in this shield to allow the anode to be placed close to the photocathode and to insert the puck into the core. The shield is made from two semi-cylindrical pieces with slightly different radii as shown in figure 4. 2. This is done to allow for maximum pumping at the photocathode surface while minimizing the line-of-sight areas to the room temperature vacuum chamber walls. This shield is cooled by the cold He gas exhausting from the cryostat before it is collected for re-liquification.

Heat Load and Cooling Power

In figure 4.5 we show the result of the heat flow computations which were conducted to verify the static thermal design of our ASU electron gun.

The computed power conducted to the photocathode from the HV plug was 2.0 W. The power radiated from the walls was determined to be much larger in contribution than the conduction. When the photocathode reached its lowest temperatures, the computed power due to radiation was 10.2 W. The cryostat calibration states that this heat load should result in a 50.0 K temperature at the photocathode surface. This was the largest heat load on the cold internals of the gun and needed to be mitigated as much as possible.

The radiated heat is absorbed by the surfaces of the materials depending on their emissivity due to Kirchhoff's law of thermal radiation [Siegel (2001)]. Each material is polished for high voltage operation, but as an added side-benefit the material emissivity goes down for highly polished materials, mitigating the absorption of radiative heat. Implementing a cryogenic shield [Cultrera *et al.* (2018)], which is specified by the cryostat manufacturer to reach 120 K, would then reduce the power radiated on the photocathode to 7.5 W, allowing us to reach steady temperatures below 40 K.
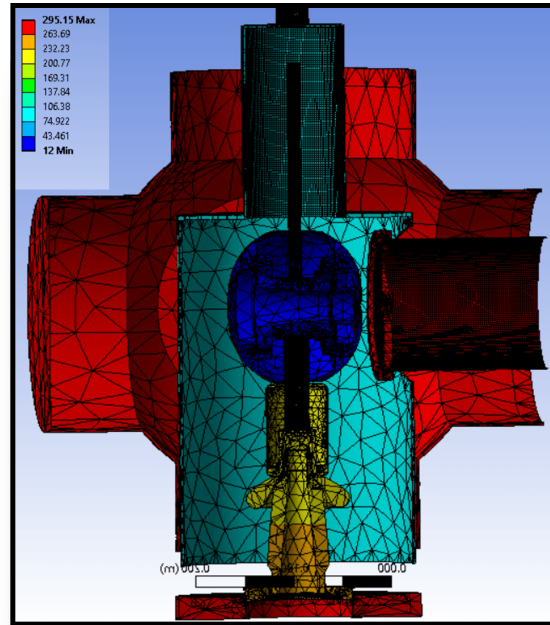
Figure 4.5: A simulation was run where sections of the gun were set to specific known temperatures and the power extraction was calculated. This cryogenic design was estimated to go to below 20 K with ideal assumptions on constant temperature sections, material thermal conductivity and material emissivity. The simulation is used to properly capture the thermal mechanics of the electron gun. The cryogenic shield maintains an intermediate temperature to block the coldest portions of the gun from the radiative heating of the room temperature chamber body.

Further reduction of radiative power and hence the photocathode temperature is possible by reducing the temperature of the cryogenic shield further by cooling it with a separate LN2 bath and by adding shutters to the photocathode transfer hole in the radiation shield.

4.3   Electron Gun Commissioning

The commissioning of the electron gun required three major phases: the polishing and assembly of the gun, the cryogenic cooling testing, and the voltage conditioning. We describe the details and results from each of these below.

4.3.1   Electron Gun Polishing and Assembly

The entire process of mirror polishing and cleaning played a vital role on the success of the voltage conditioning because any rough feature or dust particle can behave as a strong field emission source and cause voltage breakdown. We used an extensive cleaning and polishing process on all of the internal pieces of the gun. Surfaces that are exposed to large fields require such polishing to minimize the probability of field emission. Polishing the cryogenic shield improves its emissivity and therefore its ability to shield black-body radiation. A mirror-finish polishing technique was used on the electrode surfaces and the cryogenic shield based on the centrifugal barrel polishing process used at Jefferson Lab [Hernandez-Garcia *et al.* (2017)] and modified to fit our scale and budget as a university lab.

In figure 4.6 we show the tools used to reach a mirror-grade polish on the electrode surfaces and the cryogenic shield.
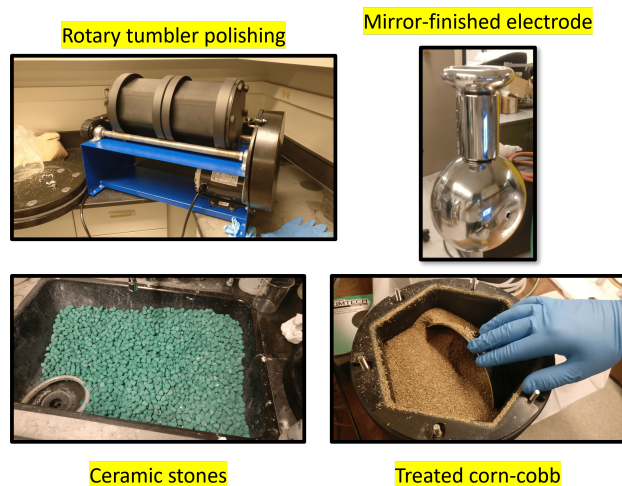
Figure 4.6: Sandpapers of 240 and 360 grit were used to roughly sand down the machined parts using DI water and isopropanol. Each piece was tossed into a tumbler with 1/2" x 9/16" ceramic cones in a 2% solution of TS compound soap to give a brushed finish. The materials were further polished with 1 200 grit sandpaper and then tossed with sharper-tipped 1/2" ceramic cones to remove the orange peel effect seen on the surfaces. Finally the materials were cleaned with isopropanol and dry-polished with treated corncob to achieve a mirror finish.

Each piece was thoroughly hand washed to remove any residual oils used during fabrication using a dish soap followed by an ultrasonic cleaning in an alkaline solution. The metals were then hand polished using medium 240 and 360 grit sandpaper and isopropanol to remove machining features and sharp edges. The pieces were placed in a rotary tumbler for polishing using 1/2" x 9/16" SX Cone ceramic stones [Mass Finishing, Inc. (2022b)] in a 2% solution of TS Compound metal cleaner soap [Mass Finishing, Inc. (2022c)] and water. The metals were left with a smooth brushed finish after two days of continuous tumbling. The tumbler was a cylindrical can of diameter 15 inches rotating at a speed of 15 revolutions per minute. This is much smaller and cheaper than the heavy duty tumbler previously used for the Jefferson Lab DC gun [Hernandez-Garcia *et al.* (2017)].

Every piece was hand polished using a fine 1200 grit sandpaper and isopropanol after tumbling, leaving a blurry mirror finish. Some of the larger electron gun electrode pieces displayed bumpy features similar to that of the surface of an orange peel. Another two days of polishing was done with sharper-tipped conical ceramic stones [Mass Finishing, Inc. (2022a)] to remove these features. Every piece was cleaned within an isopropanol bath with an ultrasonic cleaner, and then placed back into the rotary tumbler with treated corncob for dry polishing. After 3 days of continuous polishing in corncob, a full mirror finish was obtained.

A flat polished piece was measured under an interferometric microscope, as shown in figure 4.7, to quantify the quality of the polish. This helped us determine the grade of mirror finish produced by this polishing method. Across a 0.1 mm stretch of the surface there was a peak to valley surface variation of 0.2 µm. The equipotential lines will be generally unaffected on this very fine surface scale. The mirror finished pieces still appeared to have some features in the form of extremely fine streaks, as seen in the microscope image. We show the tools used to reach a finer finish and remove
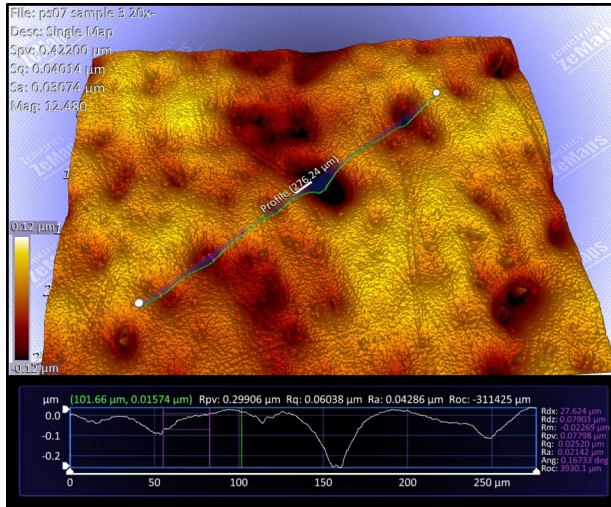
Figure 4.7: The surface slope of a mirror polished flat electrode piece was measured using an interferometric microscope at ASU. The material surface showed $0.2\,\mu m$ peak to valley surface variation over a region of $0.1\,mm$.

these features in figure 4.8. Each part was hand-scrubbed using $1.0\,\mu m$ diamond paste

Figure 4.8: Materials were further polished by hand using $1.0\,\mu m$ MetaDi diamond paste to achieve a pristine mirror surface. The paste was then cleaned off using a 150 PSI water flosser and DI water for 30 minutes per part. All parts were placed in an isopropyl bath and cleaned using a portable ultrasonic device and cleaned for 10 minutes. During assembly in a class 1000 cleanroom the materials were cleaned using a CO_2 snow-jet gun, ensuring the surfaces were contaminant free before closing the chamber.

and DI water to remove any lingering micro-features on the electrode surfaces. This was followed by 30 minutes of high-pressure rinsing (HPR) using a Homemarvel 150 PSI water flosser [HOMEMARVEL (2021)], cleaning away any microscopic diamond chunks entrapped in the electrode surface. After this process, all of the electron gun pieces were mirror finished and only needed to be cleaned for UHV assembly.

All of the UHV pieces, including the high voltage parts, were cleaned using a generic portable household ultrasonic cleaner wand in an isopropyl alcohol bath. Everything was ultrasonic cleaned for ten minutes before being taken into the cleanroom curtains for assembly. In figure 4.9 we show the completed assembly of the gun within our class 100 cleanroom environment. Inside the cleanroom, every piece was further
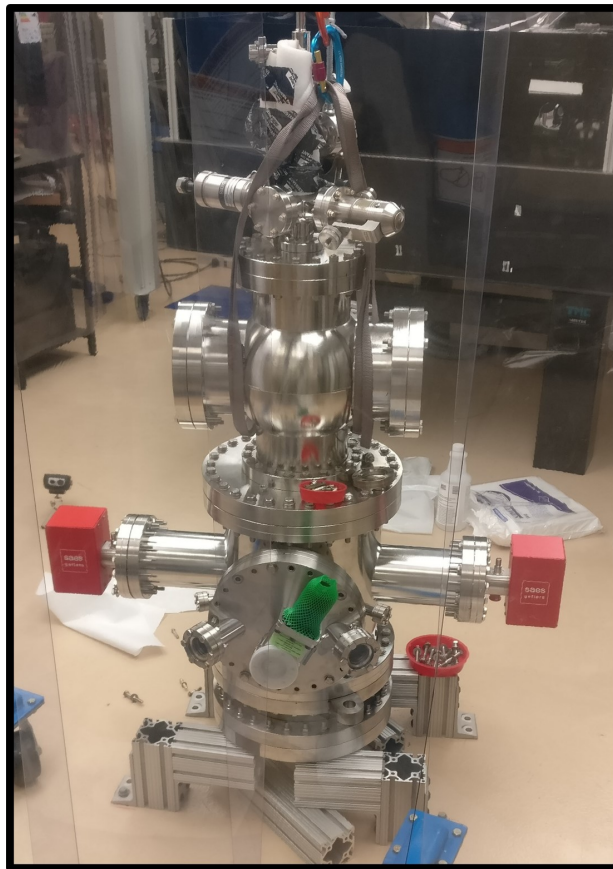
Figure 4.9: A moving cleanroom curtain with a total of eight HEPA filter conditioners was used to assemble the gun cleaning. The curtained space maintained class 100 cleanroom conditions throughout the assembly.

cleaned during assembly using a CO_2 snow-jet cleaner. This was done to ensure the insides of the chamber and the surfaces of the electrode and cryogenic shield remained dust and contaminant free.

4.3.2 Cryogenic Cooling

Cryogenic performance tests of the photocathode were done before conditioning the electron gun to high voltage. Multiple Lake Shore DT-670-SD [Lake Shore Cryotronics Inc. (2022)] cryogenic temperature sensor SI diodes were attached to the photocathode surface, electron gun core, cryogenic shielding, the sapphire rod, at the copper strap and at the cryostat end to verify the temperatures reached during the cooling process. We used a Cryomech Helium Liquifier Plant [Cryomech Inc. (2019)] to supply a continuous flow of liquid helium to the electron gun cryostat. Several steady state measurements for the photocathode temperature and the cryostat temperature were taken at various LHe flow rates while the system was under high vacuum. These measurements were used to calibrate the LHe flow rate and the cryostat end temperature to the photocathode temperature, shown in figure 4.10.
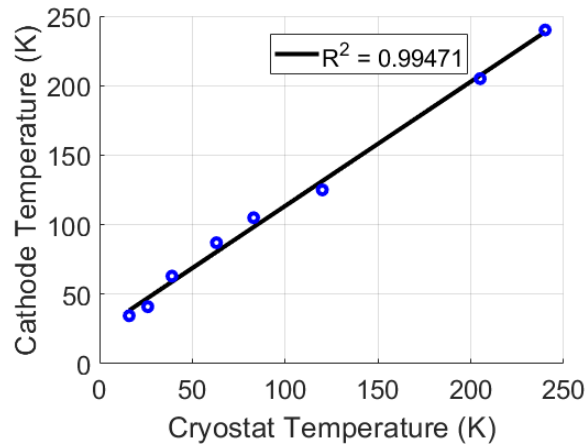
Figure 4.10: This plot shows the measured calibration between the temperature of the photocathode versus the temperature output of the cryostat. A linear-regression fit with coefficient of determination of 0.99471 is used to indirectly measure the photocathode temperature.

All diodes need to be disconnected from the high voltage components for high voltage conditioning and operation making it impractical to directly measure the photocathode temperature during high voltage operation. Hence the calibration of LHe flow and cryostat temperature vs photocathode temperature will be used to determine the photocathode temperature when the gun is operational.

We started by testing the cryogenic cooling of the photocathode without the cryogenic shield implemented to determine the performance with unmitigated black-body radiation. The room temperature chamber emits heat to the cold portions of the gun. Without the cryogenic shield the smallest photocathode temperature we achieved was 52 K with a 24 lit/day LHe flow.

We conducted a cryogenic cooling test for the assembly with the cryogenic shield layer surrounding the cold portions of the gun. In figure 4.11 we show over two days of cooling, and in this test the lowest temperature reached was 34.5 K. This temperature is able to be maintained indefinitely for cryogenic operation of the electron gun. A slight uptick can be seen in the figure near the 20 hour mark because the LHe flow rate exceeded the liquefying limit. The flow rate drifts during the initial phase of cryogenic cooling as the system properties change rapidly, and those drifts require a manual flow rate adjustment to prevent a build up of excess helium gas pressure within the recirculation pipes. Over the course of the night the system left unattended, and this resulted in a pressure build up due to flow rate drifts. A reduction of the flow rate was necessary to recover the helium pressure, and this caused the photocathode to slightly increase in temperature. The steady temperature reached at the photocathode was satisfactory for our desired use; a 34.5 K photocathode temperature translates to a 3.0 meV contribution to the MTE. This temperature contribution is low enough to reach the lowest MTE experimentally achieved to date [Karkare *et al.* (2020)] and will work for a variety for advanced photocathode tests within this electron gun. The
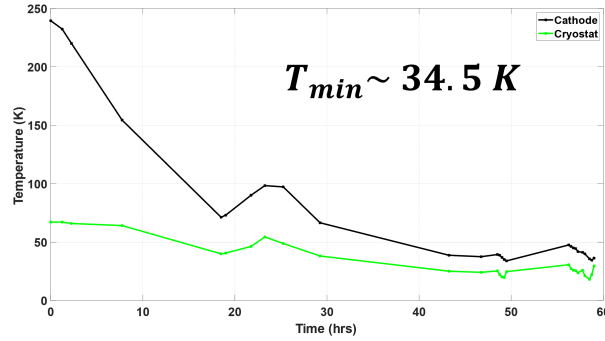
Figure 4.11: Cryogenic cooling attempted with a cryogenic shield covering the electrode. The lowest temperature of 34.5 K was reached after 48 hours of cooling, and the system was able to remain steady at this range indefinitely.

cooling time, however, was quite long, and this could cause a problem particularly for photocathodes that have sensitive surfaces and smaller lifetimes. We attempted to reduce the cooling time by nearly an order of magnitude by cooling the internals of the gun before inserting the warm photocathode puck so that the puck would "flash freeze" because it would be the only warm internal component.

In our flash freeze process the photocathode was left out of the chamber while the electron gun was cryogenically cooled over the course of two days, reaching the minimum stable temperature. The photocathode puck was then inserted into the chamber and the temperature was recorded as it cooled. Figure 4.12 shows the results of the photocathode temperature using this process. The flash freezing process yielded a rapid change of temperatures from the moment the photocathode puck was inserted into the core; the photocathode was already down from room temperature to 250 K within the first minute. The temperature of the photocathode reached 60 K after only two hours, compared to the original method taking 20 hours for the same temperature. Another 10 hours would be needed to achieve the coldest steady temperature according to our measurement shown in figure 4 .11. A photocathode lattice temperature of 60 K corresponds to a thermal limit of 5.1 meV MTE, so we conclude that this technique can be safely attempted in this electron gun using
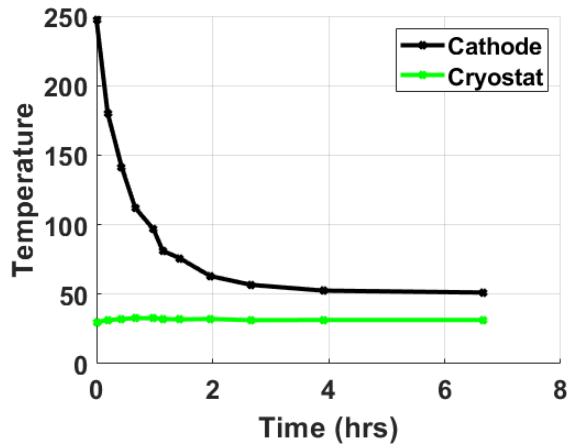
Figure 4.12: The puck at room temperature was inserted into the pre-cooled electron gun. This flash freezing process repeatedly yielded a temperature in the range of 60 K at the photocathode over the course of 2 hours. Further optimizing the mass of each electrode piece would greatly reduce the heat load and therefore reduce the total cooling time of the electron gun.

photocathodes with shorter lifetimes. For time limitation reasons, a longer test was not run.

4.3.3   High Voltage Conditioning

High voltage conditioning of the electron gun was done at room temperature after we removed all of the temperature diodes, cleaned the pieces of the gun, and reassembled them in our cleanroom. The electron gun cannot reach 200 kV immediately due to electric breakdown events which can permanently damage the gun and require cleaning or replacement of parts. Short arcing events occur before complete voltage breakdown, and these can burn off unwanted field emitters which would otherwise limit the electron gun voltage. We condition the gun to high voltage by carefully increasing the voltage and inducing short arcing events to clean our the unwanted field emitters.

A Cockcroft-Walton Multiplier HV stack was used as the high voltage power supply (HVPS) for the electron gun, the XP Power OS series 250 kV 8.0 kW model

69

[XP Power (2022)]. The stack was assembled into a tank which was later filled with sulfur hexafluoride (SF_6) dielectric gas for safe use within the lab. A HV type R28 cable from Dielectric Sciences which is rated for operation up to 225 kV [Dielectric Sciences, Inc. (2022)] was used to connect the HVPS to the electron gun. The high voltage plug was inserted with a heavy coating of dielectric grease to connect the electron gun to the output voltage of the multiplier stack. When the tank is at air, the high voltage stack is able to operate in air with 8 feet clearance from all sides. However when operated within a tank filled with the SF_6 dielectric gas, the operating footprint is 5 feet tall and 3 feet wide therefore taking up a much less space in the lab.

During the high voltage conditioning process the power supply voltage and current were controlled and monitored via 0-10 V analog signals. The pressure in the gun chamber and the radiation measured by a Geiger counter behind the gun were also monitored. Any arcing or field emission during the high voltage conditioning process causes the pressure in the gun chamber and the radiation to spike. The pressure was in the low 10^{-10} torr range when conditioning began. The voltage was increased slowly while maintaining the gun pressure below 10^{-7} torr and the radiation below 0.2 mR/hr. A LabView program was used to monitor these and control the gun voltage. The program automatically set the gun voltage to zero if any of these limits in pressure or radiation were exceeded.

We controlled the arcing activity within the electron gun by monitoring the pressure spikes on the ion pump, maintaining pressures below 10^{-7} torr throughout the process. We additionally monitored and controlled the radiation spikes by using a Geiger counter placed next to the gun chamber, maintaining radiation levels below 0.2 mR/h. We use LabView to remotely set the voltage of the stack and to record the voltage, the current, the pressure, and the radiation with each having a fail-safe

limit. The program indicates when the system is on, and will set the voltage to zero when any of the fail-safe limits have been reached.

The results of the conditioning are displayed in figure 4.13. The gun was able to immediately reach near 100 kV without many short arcing events. Pressure spikes were initially the main reason for power supply tripping, followed by current and radiation spikes as we reached up to the 200 kV range.
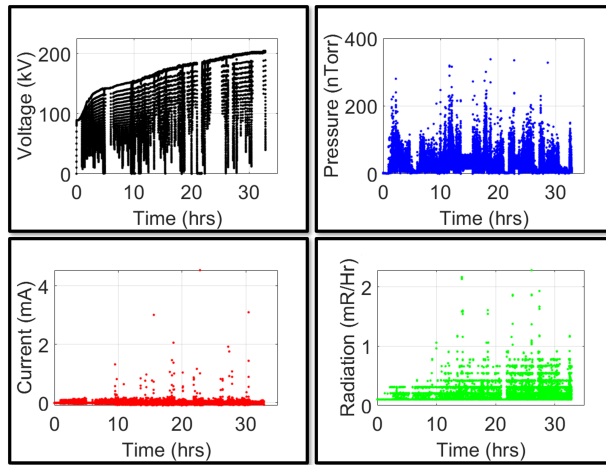
Figure 4.13: The gun high voltage (black), current (red), pressure (blue), and radiation (green) were plotted over the several hours of conditioning. The voltage reached over 200 kV after 30 hours of high voltage conditioning. Pressure spikes were the main limiter for the first 150 kV. Power supply trips due to radiation spikes became more prominent at the higher voltages.

The gun reached a steady 200 kV after 30 hours of total processing time. This processing time is very much comparable to the previous 200 kV electron guns built with similar electrostatic designs [Lee *et al.* (2018)]. This demonstrates that the polishing and cleaning process we followed using simple equipment easily available in a standard university lab space is sufficient for developing 200 kV electron guns.

4.4 Conclusion

The ASU electron gun will be used to test advanced photocathode materials in the optimal photoemission conditions. Many factors can be tuned or varied in the

electron gun as desired, including the laser wavelength and fluence, the laser beam input angle, the photocathode temperature, and the gun voltage. This gun can test the performance of a wide variety of advanced photocathode materials, such as single-crystalline, ordered surface Cu (100) and Ag (111), epitaxial grown alkali-antimonides, Dirac semimetals, and more. Material testing can be verified with surface characterization done before and after beam extraction tests in the gun [Knill *et al.* (2019)].

We will use a 500 kHz repetition rate femtosecond pulsed laser with a FWHM pulse length of 150 fs generated from a pulsed Optical Parametric Amplifier (Light Conversion Pharos pump laser with the Light Conversion Orpheus optical parametic amplifier). The laser beam will be focused through a 250 mm fused silica plano-convex lens to minimize the laser spot at the photocathode surface. The design, fabrication, preparation, and commissioning of this electron gun were all done at ASU. All of the unique features of the ASU electron gun will make this instrument excellent for testing photocathodes at high voltages. In chapter 5 we will describe a photoemission diagnostics beamline which will be used to measure advanced photocathodes.

4.5 Acknowledgements

REFERENCES

Adderley, P. A., J. Clark, J. Grames, J. Hansknecht, K. Surles-Law, D. Machie, M. Poelker, M. L. Stutzman and R. Suleiman, "Load-locked dc high voltage gaas photogun with an inverted-geometry ceramic insulator", Phys. Rev. ST Accel.

Beams **13**, 010101, URL `https://link.aps.org/doi/10.1103/PhysRevSTAB.13.010101` (2010).

Alesini, D., A. Battisti, M. Ferrario, L. Foggetta, V. Lollo, L. Ficcadenti, V. Pettinacci, S. Custodio, E. Pirez, P. Musumeci and L. Palumbo, "New technology based on clamping for high gradient radio frequency photogun", Phys. Rev. ST Accel. Beams **18**, 092001, URL `https://link.aps.org/doi/10.1103/PhysRevSTAB.18.092001` (2015).

Conde, M. *et al.*, "Research Program and Recent Results at the Argonne Wakefield Accelerator Facility (AWA)", in "Proc. IPAC'17", No. 8 in International Particle Accelerator Conference, pp. 2885–2887 (JACoW, Geneva, Switzerland, 2017).

Cryomech Inc., "Liquid helium plants and helium recovery systems", URL `https://www.cryomech.com/liquid-helium-plants/` (2019).

Cultrera, L., J. K. Bae, A. Bartnik, I. Bazarov, R. Doane, A. Galdi, C. Gulliford, W. Li, J. Maxson, S. McBride *et al.*, "Photocathodes r&d for high brightness and highly polarized electron beams at cornell university", in "Proc. IPAC'18", p. 1601–1604 (2018), URL `https://epaper.kek.jp/ipac2018/papers/tupml028.pdf`.

Dielectric Sciences, Inc., "Industrial x-ray high voltage rubber plugs receptacles dielectric sciences", URL `https://catalog.dielectricsciences.com/item/industrial-x-ray-interconnect-systems/rubber-plugs/item-1302` (2022).

Dobrovinskaya, E. R., L. A. Lytvynov and V. Pishchik, *Sapphire material, manufacturing, applications* (Springer US, 2009).

Dunham, B., J. Barley, A. Bartnik, I. Bazarov, L. Cultrera, J. Dobbins, G. Hoffstaetter, B. Johnson, R. Kaplan, S. Karkare, V. Kostroun, Y. Li, M. Liepe, X. Liu, F. Loehl, J. Maxson, P. Quigley, J. Reilly, D. Rice, D. Sabol, E. Smith, K. Smolenski, M. Tigner, V. Vesherevich, D. Widger and Z. Zhao, "Record high-average current from a high-brightness photoinjector", Appl. Phys. Lett. **102**, 3 (2013).

Filippetto, D. and H. Qian, "Design of a high-flux instrument for ultrafast electron diffraction and microscopy", J. Phys. B: At. Mol. Opt. Phys. **49**, 10, 104003 (2016).

Gevorkyan, G. S., C. Cardenas, A. Kachwala, C. Knill, T. J. Hanks and S. Karkare, "Design of a 200 kv dc cryocooled photoemission gun for photocathode investigations", in "Proc. NAPAC'22", pp. 292–295 (JACoW Publishing, Geneva, Switzerland, 2022), URL `https://jacow.org/napac2022/papers/TUYD6.pdf`.

Gevorkyan, G. S., S. S. Karkare, I. V. Bazarov, L. Cultrera, A. Galdi, W. H. Li and J. M. Maxson, "Design of a 200 kv dc cryocooled photoemission gun for photocathode investigations", in "Proc. NAPAC'19", pp. 136–139 (JACoW Publishing, Geneva, Switzerland, 2019), URL `https://jacow.org/napac2019/papers/MOPLM16.pdf`.

Gordon, M., W. H. Li, M. B. Andorf, A. C. Bartnik, C. J. R. Duncan, M. Kaemingk, C. A. Pennington, I. V. Bazarov, Y.-K. Kim and J. M. Maxson, "Four-dimensional emittance measurements of ultrafast electron diffraction optics corrected up to sextupole order", Phys. Rev. Accel. Beams **25**, 084001, URL `https://link.aps.org/doi/10.1103/PhysRevAccelBeams.25.084001` (2022).

Halbach, K., "Superfish - a computer program for evaluation of rf cavities with cylindrical symmetry", Part. Accel. **7**, 213 (1976).

Hernandez-Garcia, C., P. Adderley, B. Bullard, J. Benesch, J. Grames, J. Gubeli, F. Hannon, J. Hansknecht, J. Jordan, R. Kazimi *et al.*, "Compact- 300 kv dc inverted insulator photogun with biased anode and alkali-antimonide photocathode", Phys. Rev. Accel. Beams **22**, 11, 113401 (2019).

Hernandez-Garcia, C., D. Bullard, F. Hannon, Y. Wang and M. Poelker, "High voltage performance of a dc photoemission electron gun with centrifugal barrel-polished electrodes", Rev. Sci. Instrum. **88**, 9, 093303, URL `https://doi.org/10.1063/1.4994794` (2017).

Hernandez-Garcia, C., M. Poelker and J. Hansknecht, "High voltage studies of inverted-geometry ceramic insulators for a 350 kv dc polarized electron gun", IEEE Trans. Dielectr. Electr. Insul. **23**, 1, 418–427 (2016).

HOMEMARVEL, "Water Flossers for Teeth, 1000ML Oral Irrigator for Teeth, Electric Dental Flosser with 6 Tips,Stepless Pressure Settings(30-150PSI) , Professional for Teeth,Gums,Braces,Dental Care,Black", URL `http://www.amazon.com`, b09DSG6GVK (2021).

John, J. E. and J. J. Hilliard, *Power Transistor Cooling in a Space Environment* (National Aeronautics and Space Administration, 1963).

Karkare, S., G. Adhikari, W. A. Schroeder, J. K. Nangoi, T. Arias, J. Maxson and H. Padmore, "Ultracold electrons via near-threshold photoemission from single-crystal cu(100)", Phys. Rev. Lett. **125**, 054801, URL `https://link.aps.org/doi/10.1103/PhysRevLett.125.054801` (2020).

Karkare, S., J. Feng, X. Chen, W. Wan, F. J. Palomares, T.-C. Chiang and H. A. Padmore, "Reduction of intrinsic electron emittance from photocathodes

using ordered crystalline surfaces", Phys. Rev. Lett. **118**, 164802, URL `https://link.aps.org/doi/10.1103/PhysRevLett.118.164802` (2017).

Karkare, S., J. Feng, J. Maxson and H. A. Padmore, "Development of a 3-d energy-momentum analyzer for mev-scale energy electrons", Rev. Sci. Instrum. **90**, 5, 053902, URL `https://doi.org/10.1063/1.5091683` (2019).

Knill, C. J., J. V. Conway, B. M. Dunham, S. S. Karkare, H. A. Padmore and K. W. Smolenski, "Design of the asu photocathode lab", in "Proc. NAPAC'19", pp. 132–135 (JACoW Publishing, Geneva, Switzerland, 2019), URL `https://jacow.org/napac2019/papers/MOPLM15.pdf`.

Kurt J. Lesker Company, "ConFlat (CF) UHV Flanges & Components Technical Notes", URL `https://www.lesker.com/newweb/flanges/flanges_technicalnotes_conflat_1.cfm` (2022).

Lake Shore Cryotronics Inc., "Dt-670 silicon diodes", URL `https://www.lakeshore.com/products/categories/overview/temperature-products/cryogenic-temperature-sensors/dt-670-silicon-diodes` (2022).

Lee, H., X. Liu, L. Cultrera, B. Dunham, V. O. Kostroun and I. V. Bazarov, "A cryogenically cooled high voltage dc photoemission electron source", Rev. Sci. Instrum. **89**, 8, 083303, URL `https://doi.org/10.1063/1.5024954` (2018).

Li, W. H., C. J. R. Duncan, M. B. Andorf, A. C. Bartnik, E. Bianco, L. Cultrera, A. Galdi, M. Gordon, M. Kaemingk, C. A. Pennington, L. F. Kourkoutis, I. V. Bazarov and J. M. Maxson, "A kiloelectron-volt ultrafast electron micro-diffraction apparatus using low emittance semiconductor photocathodes", Struct. Dyn. **9**, 2, 024302, URL `https://doi.org/10.1063/4.0000138` (2022).

Manini, P. and E. Maccallini, "NEG pumps: Sorption mechanisms and applications", in "CERN Course on Vacuum for Particle Accelerators", (2017).

Mass Finishing, Inc., "1/2" x 5/8" dura 30 cone", URL `https://massfin.com/shop/ceramic-media/ceramic-cone-media/1-2-x-5-8-dura-30-cone/`, 5500-10320 (2022a).

Mass Finishing, Inc., "1/2" x 9/16" sx cone", URL `https://massfin.com/shop/synthetic-cone-media/1-2-x-9-16-sx-cone/`, 5500-10370 (2022b).

Mass Finishing, Inc., "Ts compound- 5 gallon bucket", URL `https://massfin.com/shop/chemical-compounds/t-s-compound-5-gallon-bucket/`, 5400-10002 (2022c).

Maxson, J., I. Bazarov, B. Dunham, J. Dobbins, X. Liu and K. Smolenski, "Design, conditioning, and performance of a high voltage, high brightness dc photoelectron gun with variable gap", Rev. Sci. Instrum. **85**, 9, 093306 (2014).

Miller, M. and E. Kenik, "Atom probe tomography: A technique for nanoscale characterization", Microscopy and Microanalysis **10**, 3, 336–341 (2004).

Nagai, R., R. Hajima, N. Nishimori, T. Muto, M. Yamamoto, Y. Honda, T. Miyajima, H. Iijima, M. Kuriki, M. Kuwahara *et al.*, "High-voltage testing of a 500-kv dc photocathode electron gun", Rev. Sci. Instrum. **81**, 3, 033304 (2010).

Precision Sapphire Technologies, Ltd., "Sapphire tubes, rods, spheres and special shapes", URL `https://www.sapphire.lt/products/tubes.shtml` (2022).

Rosenzweig, J., A. Cahill, B. Carlsten, G. Castorina, M. Croia, C. Emma, A. Fukusawa, B. Spataro, D. Alesini, V. Dolgashev, M. Ferrario, G. Lawler, R. Li, C. Limborg, J. Maxson, P. Musumeci, R. Pompili, S. Tantawi and O. Williams,

"Ultra-high brightness electron beams from very-high field cryogenic radiofrequency photocathode sources", Nucl. Instrum. Methods Phys. Res., Sect. A **909**, 224–228, URL `https://www.sciencedirect.com/science/article/pii/S0168900218300780`, 3rd European Advanced Accelerator Concepts workshop (EAAC2017) (2018).

SAES Getters S.p.A., "Nextorr neg - ion combination pump", URL `https://www.saesgetters.com/products/nextorr-pumps` (2022).

Sannibale, F., D. Filippetto, C. F. Papadopoulos, J. Staples, R. Wells, B. Bailey, K. Baptiste, J. Corlett, C. Cork, S. De Santis, S. Dimaggio, L. Doolittle, J. Doyle, J. Feng, D. Garcia Quintas, G. Huang, H. Huang, T. Kramasz, S. Kwiatkowski, R. Lellinger, V. Moroz, W. E. Norum, H. Padmore, C. Pappas, G. Portmann, T. Vecchione, M. Vinco, M. Zolotorev and F. Zucca, "Advanced photoinjector experiment photogun commissioning results", Phys. Rev. ST Accel. Beams **15**, 103501, URL `https://link.aps.org/doi/10.1103/PhysRevSTAB.15.103501` (2012).

Scienta Omicron GmbH, "Flag style sample plate tribus spm (molybdenum) set of 3", URL `https://scientaomicron.com/`, pN07178-S (2023).

Siegel, R., *Thermal radiation heat transfer* (CRC press, 2001).

Siggins, T., C. Sinclair, C. Bohn, D. Bullard, D. Douglas, A. Grippo, J. Gubeli, G. Krafft and B. Yunn, "Performance of a dc gaas photocathode gun for the jefferson lab fel", Nucl. Instrum. Methods Phys. Res., Sect. A **475**, 1, 549–553, URL `https://www.sciencedirect.com/science/article/pii/S0168900201015960` (2001).

Stoffel, N. and P. Johnson, "A low-energy high-brightness electron gun for inverse pho-
toemission", Nucl. Instrum. Methods Phys. Res., Sect. A **234**, 2, 230–234 (1985).

Stäubli International AG, "Multilam technology and products", URL
`https://www.staubli.com/global/en/electrical-connectors/products/`
`multilam-products-and-technology.html` (2019).

Technology Applications, Inc., "Cryocooler series (cs) cuts thermal straps
for cryocoolers / cryorefrigerators", URL `https://www.techapps.com/`
`cryocooler-series-thermal-straps` (2022).

van der Geer, S. and M. de Loos, "Applications of the general particle tracer code", in
"Proceedings of the 1997 Particle Accelerator Conference (Cat. No.97CH36167)",
vol. 2, pp. 2577–2579 vol.2 (1997).

XP Power, "Os series", URL `https://www.xppower.com/product/OS-Series?m=`
`OS250N08.0` (2022).

Chapter 5

PHASE SPACE MEASUREMENTS OF AN ELECTRON BEAM USING THE ASU CRYOCOOLED 200 KV DC ELECTRON GUN

ABSTRACT

The cryocooled DC electron gun at Arizona State University is the first electron gun built to implement single-crystal, ordered surface and epitaxially grown photocathodes to produce cold and dense electron beams at the source. This chapter presents the developments of a photocathodes characterization beamline which will be used for measurements such as emittance, response-time, and current. Detailed in this chapter is a full four-dimensional transverse phase space of the electron beam, measured using a Pinhole Scan technique developed at Cornell University. This method is used to directly calculate the mean transverse emittance in both dimensions. This chapter reports the first results of a full four-dimensional transverse phase space measurement on a molybdinum mounted alkali-antimonide photocathode, and discusses the future plans for measurements on the beamline.

5.1   Introduction

As described in chapter 4, a cryogenically cooled 200 kV DC electron gun has been commissioned at ASU [Gevorkyan *et al.* (2019, 2022)] with an objective to test such advanced photocathodes. In section 5.2 we describe the accompanying photocathode diagnostics beamline that we have built for photocathode characterization. We will describe some of the possible experiments which can be done using this tool, In section 5.3 we go into detail on the simulations of the full 4D transverse phase space measurement, and demonstrate this technique for the first time using our newly commissioned electron gun [Gevorkyan *et al.* (2023)].

5.2   The Pinhole Scan Technique for Full 4D Phase Space Measurements

In Fig. 5.1 we show the current accelerator beamline with various elements highlighted for clarity. The beamline consists of 8 corrector dipole magnets to steer the
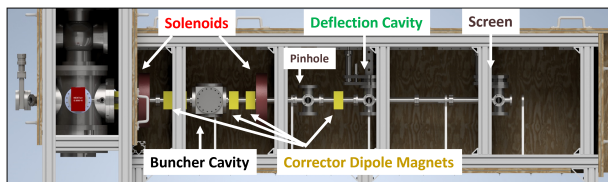
Figure 5.1: The beamline consists of corrector dipole magnets (yellow), two solenoid magnets (red), a 3.0 GHz buncher cavity, a "Pinhole" aperture element, a 3.0 GHz deflection cavity, and multiple YAG screens.

electron beam, two solenoid magnets for transverse focusing, an aperture element, a 3.0 GHz buncher cavity of the Eindhoven design [Oudheusden, van (2010)] for longitudinal focusing, and a 3.0 GHz deflection c avity. T he fi nal el ement is a YAG:Ce scintillator screen coupled to a CMOS camera and lens. In this beamline we plan to implement a solenoid scan emittance measurement [Bazarov *et al.* (2008)], a time response measurement [Bazarov *et al.* (2008)], a beam cropping phase space measurement [Ji *et al.* (2019); Gordon *et al.* (2022)], and eventually UED in the stroboscopic and single-shot modes [Ruan *et al.* (2001); Zewail (2006); Van Oudheusden *et al.*

(2010)].

The emittance in equation 1.2 is a critically important measurement of an electron beam in relation to the beam brightness in equation 1.1. To find emittance, we use a Pinhole Scan technique to measure the full 4D phase space using an aperture element to select a section of the focused electron beam and illuminate a detector screen after some drift space. This technique was developed at the MEDUSA beamline in Cornell University [Li *et al.* (2022); Gordon *et al.* (2022); Duncan *et al.* (2022)]. An illustration of the technique is shown in Fig. 5.2.
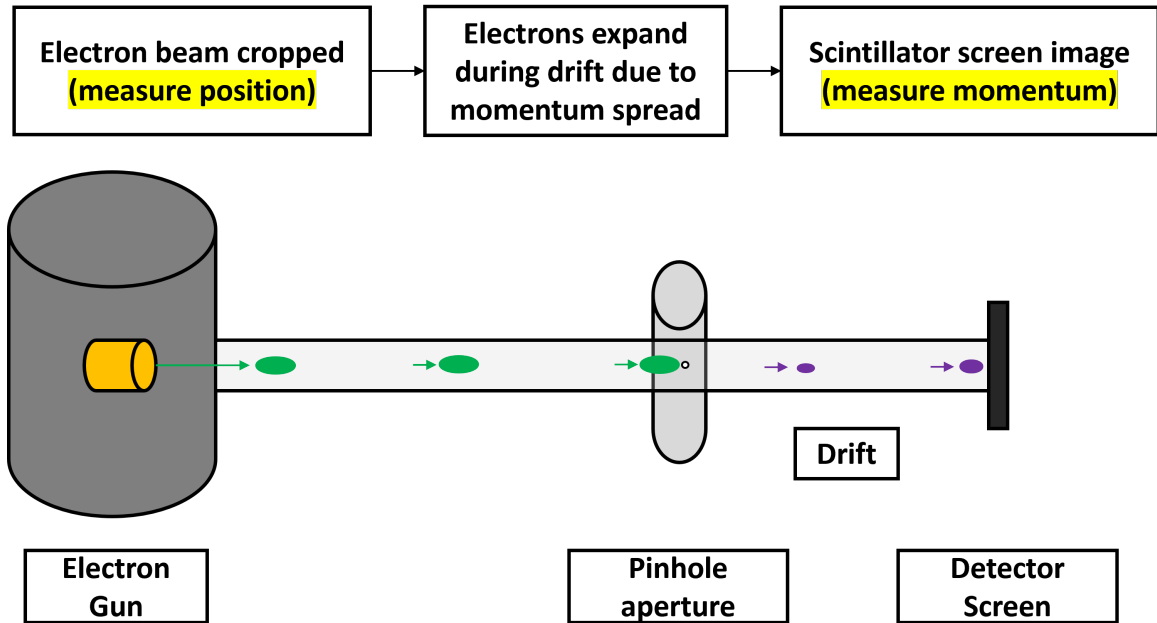
Figure 5.2: This is an illustration of the Pinhole Scan technique. Beam position is measured at the aperture, and the momentum spread is measured after a drift space.

In our beamline we use a thin tantalum foil with $10\,\mu m$, $30\,\mu m$, and $80\,\mu m$ apertures to crop to a small portion of the focused electron beam. After the beam is cropped, the electrons pass through a drift space before they reach the scintillator screen which allows us to measure the transverse momentum spread. The phase space measured will give us enough information to calculate the 4D beam matrix, which is the two RMS transverse positions and momenta and their related correlations.

$$\Sigma_{4D} = \begin{bmatrix} \langle xx \rangle & \langle xx' \rangle & \langle xy \rangle & \langle xy' \rangle \\ \langle x'x \rangle & \langle x'x' \rangle & \langle x'y \rangle & \langle x'y' \rangle \\ \langle yx \rangle & \langle yx' \rangle & \langle yy \rangle & \langle yy' \rangle \\ \langle y'x \rangle & \langle y'x' \rangle & \langle y'y \rangle & \langle y'y' \rangle \end{bmatrix}. \tag{5.1}$$

In the equation, x and y represent the transverse position of the beam at the aperture, and the primed coordinates are derivatives with respect to longitudinal position and represent the transverse momentum. We use this matrix to calculate the 4D normalized emittance and determine the mean transverse energy (MTE) of the beam.

$$\epsilon_{4D,n} = (\gamma\beta)^2 \sqrt{\det(\Sigma_{4D})}, \tag{5.2}$$

where det is the determinant of the matrix. The 4D emittance can then be used to find the electron beam MTE,

$$\text{MTE} = \frac{\epsilon_{4D,n}}{\sigma_i^2 m_0 c^2}. \tag{5.3}$$

In this equation σ_i is the RMS laser spot size and $m_0 c^2$ is the rest mass energy of a free electron.

5.3 Implementing the Pinhole Scan at the ASU Cryogun Beamline

5.3.1 Simulations of Phase Space Measurements

We modeled this Pinhole Scan technique in GPT [van der Geer and de Loos (1997)] and analyzed the results in MATLAB. We simulated our expected beam parameters and real beamline elements to compute an image comparable to our real detector screen and CMOS camera. The beam was rastered over the aperture by adjusting the simulated corrector coils. We then used MATLAB to compute the full 4D phase

space of the beam using the resulting images of the simulation. Using simulation, have predicted results for a large range of values for MTEs and beam spot sizes we expect to measure.

The smallest emittance that can be measured is limited by the aperture used, the resolution of the screen and camera system, and the distance between the aperture and the screen. In our setup the drift distance is 0.7 m. For this drift a 1.0 µm spot on the screen corresponds to a transverse momentum of 0.30 eV/c. Assuming a 50 µm resolution of the YAG screen and the camera-lens imaging system, we get a precision of of 14.97 eV/c in the measured σ_{px}. If we use the 10 µm aperture, the smallest possible emittance that can be measured is 0.53 nm-rad.

5.3.2   Measurements on the Beamline

In Fig 5.3 we show a Pinhole Scan of a beam from a Cs_3Sb photocathode on a molybdenum substrate. This photocathode was significantly degraded since it had been in the electron gun for over two months since growth. A 532 nm continuous laser with 5 mW power was focused to the center 100 µm of the photocathode. A flip mirror was used to direct the laser beam to a intensity profiler matching the distance to the photocathode to measure the laser spot size, which was measured to be 70 µm RMS. The beam was focused and centered onto the 80 µm aperture. We rastered the beam in small steps using an advanced optimized scanning strategy to suppress errors due to systematic drift [Emma *et al.* (2010); Pellegrini (2012)]. Each image was 811-by-811 pixels and the resolution was 13.636 µm per pixel. Our MATLAB code interpreted these images to compute the matrix in equation 5.1 and emittance in equation 5.2. Using equation 5.3 we measured an MTE of 76.6 meV for our degraded Cs_3Sb sample using 532 nm light.
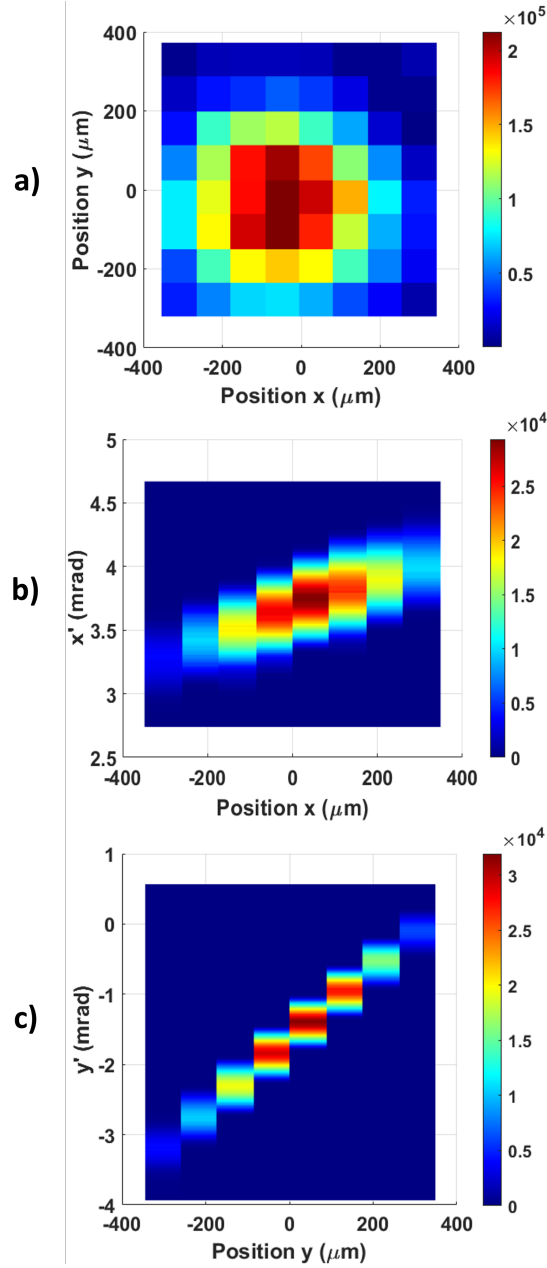
Figure 5.3: A full 4D phase space was reconstructed from our degraded Cs_3Sb photocathode grown on molybdenum using the pinhole scan technique. This was measured in our beamline at 30 keV with a spot size of 70 µm. We show the transverse positions x-y (5.3a), where $\sigma_x = 158.53$ µm and $\sigma_y = 151.02$ µm. In (5.3b) and (5.3c) we plot the 2D phase space in one transverse axes x-x' and y-y' respectively, $\sqrt{\epsilon_{4d}} = 27.1$ nm-rad.

5.4   Conclusion

Future automation of this code can be implemented to remove as much of the manual operation of the beam as possible, particularly in the dipole coil momentum calibration and in the actual measurement process. Testing single-crystalline photocathodes at cryogenic temperatures will be a priority because they have demonstrated record low transverse energy spreads, and measuring the full 4D phase space of such materials at high voltage in optimal conditions is currently only possible using this electron gun and beamline.

Cryogenic cooling was not used because the laser was significantly above threshold energy for Cs_3Sb. The next iteration of this beamline will use our tunable wavelength laser, which has a 500 kHz repetition rate and a FWHM pulse length of 150 fs from a pulsed Optical Parametric Amplifier. We expect to see a difference in the emittance after tuning the wavelength to threshold and cryogenically cooling the photocathode [Karkare *et al.* (2017)]. This beamline will eventually be used for UED in both the stroboscopic and single-shot modes[Oudheusden, van (2010); Van Oudheusden *et al.* (2010, 2007); Li *et al.* (2010); Duncan *et al.* (2022)], making it possible to surpass the k-space resolution of existing UED tools, given proper beam quality preservation, due to the ability to make use of higher brightness sources in our electron gun.

5.5   Acknowledgements

REFERENCES

Bazarov, I. V., B. M. Dunham, Y. Li, X. Liu, D. G. Ouzounov, C. K. Sinclair, F. Hannon and T. Miyajima, "Thermal emittance and response time measurements of negative electron affinity photocathodes", J. Appl. Phys. **103**, 5, 054901, URL `https://doi.org/10.1063/1.2838209` (2008).

Duncan, C. J. R., M. Kaemingk, W. H. Li, M. B. Andorf, A. C. Bartnik, A. Galdi, M. Gordon, C. A. Pennington, I. V. Bazarov, H. J. Zeng, F. Liu, D. Luo, A. Sood, A. M. Lindenberg, M. W. Tate, D. A. Muller, J. Thom-Levy, S. M. Gruner and J. M. Maxson, "Multi-scale time-resolved electron diffraction enabled by high repetition rate, high dynamic range direct electron detection", (2022).

Emma, P., R. Akre, J. Arthur, R. Bionta, C. Bostedt, J. Bozek, A. Brachmann, P. Bucksbaum, R. Coffee, F.-J. Decker *et al.*, "First lasing and operation of an ångstrom-wavelength free-electron laser", Nat. Photonics **4**, 9, 641–647 (2010).

Gevorkyan, G., C. Sarabia Cardenas *et al.*, "Phase space measurements of an electron beam using the asu cryocooled 200 kv dc electron gun", in "Proc. IPAC'23", No. 14 in IPAC'23 - 14th International Particle Accelerator Conference, pp. 1365–1369 (JACoW Publishing, Geneva, Switzerland, 2023).

Gevorkyan, G. S., C. Cardenas, A. Kachwala, C. Knill, T. J. Hanks and S. Karkare, "Design of a 200 kv dc cryocooled photoemission gun for photocathode investigations", in "Proc. NAPAC'22", pp. 292–295 (JACoW Publishing, Geneva, Switzerland, 2022), URL `https://jacow.org/napac2022/papers/TUYD6.pdf`.

Gevorkyan, G. S., S. S. Karkare, I. V. Bazarov, L. Cultrera, A. Galdi, W. H. Li and J. M. Maxson, "Design of a 200 kv dc cryocooled photoemission gun for photocathode investigations", in "Proc. NAPAC'19", pp. 136–139 (JACoW Publishing, Geneva, Switzerland, 2019), URL `https://jacow.org/napac2019/papers/MOPLM16.pdf`.

Gordon, M., W. H. Li, M. B. Andorf, A. C. Bartnik, C. J. R. Duncan, M. Kaemingk, C. A. Pennington, I. V. Bazarov, Y.-K. Kim and J. M. Maxson, "Four-dimensional emittance measurements of ultrafast electron diffraction optics corrected up to sextupole order", Phys. Rev. Accel. Beams **25**, 084001, URL `https://link.aps.org/doi/10.1103/PhysRevAccelBeams.25.084001` (2022).

Ji, F., J. G. Navarro, P. Musumeci, D. B. Durham, A. M. Minor and D. Filippetto, "Knife-edge based measurement of the 4d transverse phase space of electron beams with picometer-scale emittance", Phys. Rev. Accel. Beams **22**, 082801, URL `https://link.aps.org/doi/10.1103/PhysRevAccelBeams.22.082801` (2019).

Karkare, S., J. Feng, X. Chen, W. Wan, F. J. Palomares, T.-C. Chiang and H. A. Padmore, "Reduction of intrinsic electron emittance from photocathodes using ordered crystalline surfaces", Phys. Rev. Lett. **118**, 164802, URL `https://link.aps.org/doi/10.1103/PhysRevLett.118.164802` (2017).

Li, R., W. Huang, Y. Du, L. Yan, Q. Du, J. Shi, J. Hua, H. Chen, T. Du, H. Xu *et al.*, "Note: Single-shot continuously time-resolved mev ultrafast electron diffraction", Rev. Sci. Instrum. **81**, 3, 036110 (2010).

Li, W. H., C. J. R. Duncan, M. B. Andorf, A. C. Bartnik, E. Bianco, L. Cultrera, A. Galdi, M. Gordon, M. Kaemingk, C. A. Pennington, L. F. Kourkoutis, I. V. Bazarov and J. M. Maxson, "A kiloelectron-volt ultrafast electron micro-diffraction

apparatus using low emittance semiconductor photocathodes", Struct. Dyn. **9**, 2, 024302, URL `https://doi.org/10.1063/4.0000138` (2022).

Oudheusden, van, T., *Electron source for sub-relativistic single-shot femtosecond diffraction*, Ph.D. thesis, Applied Physics (2010).

Pellegrini, C., "The history of x-ray free-electron lasers", Eur. Phys. J. H **37**, 5, 659–708 (2012).

Ruan, C.-Y., V. A. Lobastov, R. Srinivasan, B. M. Goodson, H. Ihee and A. H. Zewail, "Ultrafast diffraction and structural dynamics: The nature of complex molecules far from equilibrium", Proc. Natl. Acad. Sci. U.S.A. **98**, 13, 7117–7122 (2001).

van der Geer, S. and M. de Loos, "Applications of the general particle tracer code", in "Proceedings of the 1997 Particle Accelerator Conference (Cat. No.97CH36167)", vol. 2, pp. 2577–2579 vol.2 (1997).

Van Oudheusden, T., E. De Jong, S. Van der Geer, W. O. 't Root, O. Luiten and B. Siwick, "Electron source concept for single-shot sub-100 fs electron diffraction in the 100 kev range", J. Appl. Phys. **102**, 9, 093501 (2007).

Van Oudheusden, T., P. Pasmans, S. Van Der Geer, M. De Loos, M. Van Der Wiel and O. Luiten, "Compression of subrelativistic space-charge-dominated electron bunches for single-shot femtosecond electron diffraction", Phys. Rev. Lett. **105**, 26, 264801 (2010).

Zewail, A. H., "4d ultrafast electron diffraction, crystallography, and microscopy", Annu. Rev. Phys. Chem. **57**, 65–103 (2006).

Chapter 6

CONCLUSION

Ultra-low emittance photocathodes can pave the way to improve electron-based technologies such as XFELs and inverse Compton scattering experiments; ultrafast electron scattering techniques like UED, UEM, and U-EELS; and particle colliders for fundamental physics research. Modern photoinjectors use polycrystalline metals as their electron source and are limited on the brightness of those sources due to a variety of effects. One of these effects is likely the nanoscale surface roughnesses as we described in detail in chapter 2. Ordered surface, single crystalline photocathodes could be used in conjuction with nanoscale laser spot sizes to produce ultra-low emittance electron beams. In chapter 3 we described how such materials could perform as next generation electron sources for electron microscopes. The brightness from ultra-low emittance sources could be two orders of magnitude larger that the brightness of the best technology used today, with the added benefit of having low energy spreads without the use of a monochromator. In chapters 4 and 5 we described the development and commissioning of a high accelerating gradient, cryogenically cooled, 200 kV DC electron gun and photoemission diagnostics beamline within our photocathodes research lab. This accelerator has a unique capability to utilize photocathodes mounted on holders typically used in commercial surface chemistry tools, and furthermore has the necessary features and tools for operating in the optimal regime for many advanced photocathodes. We demonstrated a full 4D phase space measurement with this tool; this is a big step toward investigating the use of advanced photocathodes which can produce ultra-low emittance electron beams for modern photoinjector applications.

90

REFERENCES

Adderley, P. A., J. Clark, J. Grames, J. Hansknecht, K. Surles-Law, D. Machie, M. Poelker, M. L. Stutzman and R. Suleiman, "Load-locked dc high voltage gaas photogun with an inverted-geometry ceramic insulator", Phys. Rev. ST Accel. Beams **13**, 010101, URL `https://link.aps.org/doi/10.1103/PhysRevSTAB.13.010101` (2010).

Alesini, D., A. Battisti, M. Ferrario, L. Foggetta, V. Lollo, L. Ficcadenti, V. Pettinacci, S. Custodio, E. Pirez, P. Musumeci and L. Palumbo, "New technology based on clamping for high gradient radio frequency photogun", Phys. Rev. ST Accel. Beams **18**, 092001, URL `https://link.aps.org/doi/10.1103/PhysRevSTAB.18.092001` (2015).

Arnold, A. and J. Teichert, "Overview on superconducting photoinjectors", Phys. Rev. ST Accel. Beams **14**, 024801, URL `https://link.aps.org/doi/10.1103/PhysRevSTAB.14.024801` (2011).

Bazarov, I. V., B. M. Dunham, Y. Li, X. Liu, D. G. Ouzounov, C. K. Sinclair, F. Hannon and T. Miyajima, "Thermal emittance and response time measurements of negative electron affinity photocathodes", J. Appl. Phys. **103**, 5, 054901, URL `https://doi.org/10.1063/1.2838209` (2008).

Bradley, D. J., M. B. Allenson and B. R. Holeman, "The transverse energy of electrons emitted from gaas photocathodes", J. of Phys. D **10**, 111 (1977).

Brau, C., "What brightness means", in "The Physics and Applications of High Brightness Electron Beams", pp. 20–27 (World Scientific, 2003).

Brem, S., C. Linderälv, P. Erhart and E. Malic, "Tunable phases of moiré excitons in van der waals heterostructures", Nano Letters **20**, 12, 8534–8540, URL `https://doi.org/10.1021/acs.nanolett.0c03019`, pMID: 32970445 (2020).

Brunner, R., M. Burkhardt, A. Pesch, O. Sandfuchs, M. Ferstl, S. Hohng and J. O. White, "Diffraction-based solid immersion lens", JOSA A **21**, 7, 1186–1191 (2004).

Candy, J. and W. Rozmus, "A symplectic integration algorithm for separable hamiltonian functions", Journal of Computational Physics **92**, 1, 230–256 (1991).

Carbone, F., O.-H. Kwon and A. H. Zewail, "Dynamics of chemical bonding mapped by energy-resolved 4d electron microscopy", Science **325**, 5937, 181–184 (2009).

Conde, M. *et al.*, "Research Program and Recent Results at the Argonne Wakefield Accelerator Facility (AWA)", in "Proc. IPAC'17", No. 8 in International Particle Accelerator Conference, pp. 2885–2887 (JACoW, Geneva, Switzerland, 2017).

Cryomech Inc., "Liquid helium plants and helium recovery systems", URL `https://www.cryomech.com/liquid-helium-plants/` (2019).

Cultrera, L., J. K. Bae, A. Bartnik, I. Bazarov, R. Doane, A. Galdi, C. Gulliford, W. Li, J. Maxson, S. McBride *et al.*, "Photocathodes r&d for high brightness and highly polarized electron beams at cornell university", in "Proc. IPAC'18", p. 1601–1604 (2018), URL `https://epaper.kek.jp/ipac2018/papers/tupml028.pdf`.

Cultrera, L., S. Karkare, H. Lee, X. Liu, I. Bazarov and B. Dunham, "Cold electron beams from cryocooled, alkali antimonide photocathodes", Phys. Rev. ST Accel. Beams **18**, 113401, URL `https://link.aps.org/doi/10.1103/PhysRevSTAB.18.113401` (2015a).

Cultrera, L., S. Karkare, H. Lee, X. Liu, I. V. Bazarov and B. Dunham, "Quantum efficiency and thermal emittance of metal photocathodes", Physical Review Special Topics - Accelerators and Beams **18**, 113401 (2015b).

Dielectric Sciences, Inc., "Industrial x-ray high voltage rubber plugs receptacles dielectric sciences", URL `https://catalog.dielectricsciences.com/item/industrial-x-ray-interconnect-systems/rubber-plugs/item-1302` (2022).

Dobrovinskaya, E. R., L. A. Lytvynov and V. Pishchik, *Sapphire material, manufacturing, applications* (Springer US, 2009).

Dowell, D. H. and J. F. Schmerge, "Quantum efficiency and thermal emittance of metal photocathodes", Phys. Rev. ST Accel. Beams **12**, 074201, URL `https://link.aps.org/doi/10.1103/PhysRevSTAB.12.074201` (2009).

Duncan, C. J. R., M. Kaemingk, W. H. Li, M. B. Andorf, A. C. Bartnik, A. Galdi, M. Gordon, C. A. Pennington, I. V. Bazarov, H. J. Zeng, F. Liu, D. Luo, A. Sood, A. M. Lindenberg, M. W. Tate, D. A. Muller, J. Thom-Levy, S. M. Gruner and J. M. Maxson, "Multi-scale time-resolved electron diffraction enabled by high repetition rate, high dynamic range direct electron detection", (2022).

Dunham, B., J. Barley, A. Bartnik, I. Bazarov, L. Cultrera, J. Dobbins, G. Hoffstaetter, B. Johnson, R. Kaplan, S. Karkare, V. Kostroun, Y. Li, M. Liepe, X. Liu, F. Loehl, J. Maxson, P. Quigley, J. Reilly, D. Rice, D. Sabol, E. Smith, K. Smolenski, M. Tigner, V. Vesherevich, D. Widger and Z. Zhao, "Record high-average current from a high-brightness photoinjector", Appl. Phys. Lett. **102**, 3 (2013).

Durham, D. B., F. Riminucci, F. Ciabattini, A. Mostacci, A. M. Minor, S. Cabrini and D. Filippetto, "Plasmonic lenses for tunable ultrafast electron emitters at the nanoscale", Phys. Rev. Appl. **12**, 5, 054057 (2019).

Emma, P., R. Akre, J. Arthur, R. Bionta, C. Bostedt, J. Bozek, A. Brachmann, P. Bucksbaum, R. Coffee, F.-J. Decker *et al.*, "First lasing and operation of an ångstrom-wavelength free-electron laser", Nat. Photonics **4**, 9, 641–647 (2010).

Feng, J., S. Karkare, J. Nasiatka, S. Schubert, J. Smedley and H. A. Padmore, "Near atomically smooth alkali antimonide photocathode thin films", J. Appl. Phys. **121**, 044904 (2017).

Feng, J., J. Nasiatka, W. Wan, S. Karkare, J. Smedley and H. A. Padmore, "Thermal limit to the intrinsic emittance from metal photocathodes", Appl. Phys. Lett. **107**, 13, 134101, URL https://doi.org/10.1063/1.4931976 (2015).

Filippetto, D., P. Musumeci, M. Zolotorev and G. Stupakov, "Maximum current density and beam brightness achievable by laser-driven electron sources", Physical Review Special Topics-Accelerators and Beams **17**, 2, 024201 (2014).

Filippetto, D. and H. Qian, "Design of a high-flux instrument for ultrafast electron diffraction and microscopy", J. Phys. B: At. Mol. Opt. Phys. **49**, 10, 104003 (2016).

Forest, E., "Geometric integration for particle accelerators", Journal of Physics A: Mathematical and General **39**, 19, 5321 (2006).

Forest, E. and R. D. Ruth, "Fourth-order symplectic integration", Physica D: Nonlinear Phenomena **43**, 1, 105–117 (1990).

Gevorkyan, G., C. Sarabia Cardenas *et al.*, "Phase space measurements of an electron beam using the asu cryocooled 200 kv dc electron gun", in "Proc. IPAC'23", No. 14 in IPAC'23 - 14th International Particle Accelerator Conference, pp. 1365–1369 (JACoW Publishing, Geneva, Switzerland, 2023).

Gevorkyan, G. S., C. Cardenas, A. Kachwala, C. Knill, T. J. Hanks and S. Karkare, "Design of a 200 kv dc cryocooled photoemission gun for photocathode investigations", in "Proc. NAPAC'22", pp. 292–295 (JACoW Publishing, Geneva, Switzerland, 2022), URL https://jacow.org/napac2022/papers/TUYD6.pdf.

Gevorkyan, G. S., S. Karkare, S. Emamian, I. V. Bazarov and H. A. Padmore, "Effects of physical and chemical surface roughness on the brightness of electron beams from photocathodes", Phys. Rev. Accel. Beams **21**, 093401, URL https://link.aps.org/doi/10.1103/PhysRevAccelBeams.21.093401 (2018).

Gevorkyan, G. S., S. S. Karkare, I. V. Bazarov, L. Cultrera, A. Galdi, W. H. Li and J. M. Maxson, "Design of a 200 kv dc cryocooled photoemission gun for photocathode investigations", in "Proc. NAPAC'19", pp. 136–139 (JACoW Publishing, Geneva, Switzerland, 2019), URL https://jacow.org/napac2019/papers/MOPLM16.pdf.

Gordon, M., W. H. Li, M. B. Andorf, A. C. Bartnik, C. J. R. Duncan, M. Kaemingk, C. A. Pennington, I. V. Bazarov, Y.-K. Kim and J. M. Maxson, "Four-dimensional emittance measurements of ultrafast electron diffraction optics corrected up to sextupole order", Phys. Rev. Accel. Beams **25**, 084001, URL https://link.aps.org/doi/10.1103/PhysRevAccelBeams.25.084001 (2022).

Gordon, M., S. Van Der Geer, J. Maxson and Y.-K. Kim, "Point-to-point coulomb effects in high brightness photoelectron beam lines for ultrafast electron diffraction", Physical Review Accelerators and Beams **24**, 8, 084202 (2021).

Gorlov, T., "High-precision calculation of quasistatic field near a photocathode surface microrelief", J. Electrostat **65**, 735 (2007).

Graves, W., W. Brown, F. Kaertner and D. Moncton, "Mit inverse compton source concept", Nucl. Instrum. Methods Phys. Res., Sect. A **608**, 1, Supplement, S103–S105, URL `https://www.sciencedirect.com/science/article/pii/S0168900209009802`, compton sources for X/γ rays: Physics and applications (2009).

Graves, W. S., J. Bessuille, P. Brown, S. Carbajo, V. Dolgashev, K.-H. Hong, E. Ihloff, B. Khaykovich, H. Lin, K. Murari, E. A. Nanni, G. Resta, S. Tantawi, L. E. Zapata, F. X. Kärtner and D. E. Moncton, "Compact x-ray source based on burst-mode inverse compton scattering at 100 khz", Phys. Rev. ST Accel. Beams **17**, 120701, URL `https://link.aps.org/doi/10.1103/PhysRevSTAB.17.120701` (2014).

Graves, W. S., F. X. Kärtner, D. E. Moncton and P. Piot, "Intense superradiant x rays from a compact source using a nanocathode array and emittance exchange", Phys. Rev. Lett. **108**, 263904, URL `https://link.aps.org/doi/10.1103/PhysRevLett.108.263904` (2012).

Halbach, K., "Superfish - a computer program for evaluation of rf cavities with cylindrical symmetry", Part. Accel. **7**, 213 (1976).

Hastings, J., F. Rudakov, D. Dowell, J. Schmerge, J. Cardoza, J. Castro, S. Gierman, H. Loos and P. Weber, "Ultrafast time-resolved electron diffraction with megavolt electron beams", Appl. Phys. Lett. **89**, 18, 184109 (2006).

Hernandez-Garcia, C., P. Adderley, B. Bullard, J. Benesch, J. Grames, J. Gubeli, F. Hannon, J. Hansknecht, J. Jordan, R. Kazimi *et al.*, "Compact- 300 kv dc inverted insulator photogun with biased anode and alkali-antimonide photocathode", Phys. Rev. Accel. Beams **22**, 11, 113401 (2019).

Hernandez-Garcia, C., D. Bullard, F. Hannon, Y. Wang and M. Poelker, "High voltage performance of a dc photoemission electron gun with centrifugal barrel-polished electrodes", Rev. Sci. Instrum. **88**, 9, 093303, URL `https://doi.org/10.1063/1.4994794` (2017).

Hernandez-Garcia, C., M. Poelker and J. Hansknecht, "High voltage studies of inverted-geometry ceramic insulators for a 350 kv dc polarized electron gun", IEEE Trans. Dielectr. Electr. Insul. **23**, 1, 418–427 (2016).

HOMEMARVEL, "Water Flossers for Teeth, 1000ML Oral Irrigator for Teeth, Electric Dental Flosser with 6 Tips,Stepless Pressure Settings(30-150PSI) , Professional for Teeth,Gums,Braces,Dental Care,Black", URL `http://www.amazon.com`, b09DSG6GVK (2021).

Jensen, K. L., "Scattering and the relationship between quantum efficiency and emittance", J. Appl. Phys. **113**, 056101 (2013).

Jensen, K. L., D. A. Shiffler, J. J. Petillo, Z. Pan and J. W. Luginsland, "Emittance, surface structure, and electron emission", Phys. Rev. ST Accel. Beams **17**, 043402 (2014).

Ji, F., J. G. Navarro, P. Musumeci, D. B. Durham, A. M. Minor and D. Filippetto, "Knife-edge based measurement of the 4d transverse phase space of electron beams with picometer-scale emittance", Phys. Rev. Accel. Beams **22**, 082801, URL `https://link.aps.org/doi/10.1103/PhysRevAccelBeams.22.082801` (2019).

John, J. E. and J. J. Hilliard, *Power Transistor Cooling in a Space Environment* (National Aeronautics and Space Administration, 1963).

Kabius, B. C., N. D. Browning, S. Thevuthasan, B. L. Diehl and E. A. Stach, "Dynamic processes in biology, chemistry, and materials science: Opportunities for ultrafast transmission electron microscopy - workshop summary report", DOE Technical Report URL `https://www.osti.gov/biblio/1069215` (2012).

Karkare, S., G. Adhikari, W. A. Schroeder, J. K. Nangoi, T. Arias, J. Maxson and H. Padmore, "Ultracold electrons via near-threshold photoemission from single-crystal cu(100)", Phys. Rev. Lett. **125**, 054801, URL `https://link.aps.org/doi/10.1103/PhysRevLett.125.054801` (2020).

Karkare, S. and I. V. Bazarov, "Effect of nanoscale surface roughness on transverse energy spread from gaas photocathodes", Appl. Phys. Lett. **98**, 094104 (2011).

Karkare, S. and I. V. Bazarov, "Effects of surface nonuniformities on the mean transverse energy from photocathodes", Phys. Rev. Appl. **4**, 024015 (2015).

Karkare, S., D. Dimitrov, W. Schaff, L. Cultrera, A. Bartnik, X. Liu, E. Sawyer, T. Esposito and I. V. Bazarov, "Monte carlo charge transport and photoemission from negative electron affinity gaas photocathodes", J. Appl. Phys **113**, 104904 (2013).

Karkare, S., S. Emamian, G. Gevorkyan, H. A. Padmore and A. Schmidt, "Physical and chemical roughness of alkali-antimonide cathodes", Proc. IPAC'18 p. 4259, URL `http://ipac2018.vrws.de/papers/thpmf080.pdf` (2018).

Karkare, S., J. Feng, X. Chen, W. Wan, F. J. Palomares, T.-C. Chiang and H. A. Padmore, "Reduction of intrinsic electron emittance from photocathodes using ordered crystalline surfaces", Phys. Rev. Lett. **118**, 164802, URL `https://link.aps.org/doi/10.1103/PhysRevLett.118.164802` (2017).

Karkare, S., J. Feng, J. Maxson and H. A. Padmore, "Development of a 3-d energy-momentum analyzer for mev-scale energy electrons", Rev. Sci. Instrum. **90**, 5, 053902, URL `https://doi.org/10.1063/1.5091683` (2019).

Kisielowski, C., B. Freitag, M. Bischoff, H. Van Lin, S. Lazar, G. Knippels, P. Tiemeijer, M. van der Stam, S. von Harrach, M. Stekelenburg *et al.*, "Detection of single atoms and buried defects in three dimensions by aberration-corrected electron microscope with 0.5-å information limit", Microscopy and Microanalysis **14**, 5, 469–477 (2008).

Knill, C., S. Karkare and H. Padmore, "Near-Threshold Nonlinear Photoemission From Cu(100)", in "Proc. IPAC'21", No. 12 in International Particle Accelerator Conference, pp. 2822–2825 (JACoW Publishing, Geneva, Switzerland, 2021).

Knill, C. J., J. V. Conway, B. M. Dunham, S. S. Karkare, H. A. Padmore and K. W. Smolenski, "Design of the asu photocathode lab", in "Proc. NAPAC'19", pp. 132–135 (JACoW Publishing, Geneva, Switzerland, 2019), URL `https://jacow.org/napac2019/papers/MOPLM15.pdf`.

Krasilnikov, M., "Impact of the cathode roughness on the emittance of an electron beam", Proc. of FEL Conf. p. 583 (2006).

Krivanek, O. L., T. C. Lovejoy, N. Dellby, T. Aoki, R. Carpenter, P. Rez, E. Soignard, J. Zhu, P. E. Batson, M. J. Lagos *et al.*, "Vibrational spectroscopy in the electron microscope", Nature **514**, 7521, 209–212 (2014).

Kurt J. Lesker Company, "ConFlat (CF) UHV Flanges & Components Technical Notes", URL `https://www.lesker.com/newweb/flanges/flanges_technicalnotes_conflat_1.cfm` (2022).

Lake Shore Cryotronics Inc., "Dt-670 silicon diodes", URL `https://www.lakeshore.com/products/categories/overview/temperature-products/cryogenic-temperature-sensors/dt-670-silicon-diodes` (2022).

Lee, H., X. Liu, L. Cultrera, B. Dunham, V. O. Kostroun and I. V. Bazarov, "A cryogenically cooled high voltage dc photoemission electron source", Rev. Sci. Instrum. **89**, 8, 083303, URL `https://doi.org/10.1063/1.5024954` (2018).

Li, R., W. Huang, Y. Du, L. Yan, Q. Du, J. Shi, J. Hua, H. Chen, T. Du, H. Xu *et al.*, "Note: Single-shot continuously time-resolved mev ultrafast electron diffraction", Rev. Sci. Instrum. **81**, 3, 036110 (2010).

Li, R., C. Tang, Y. Du, W. Huang, Q. Du, J. Shi, L. Yan and X. Wang, "Experimental demonstration of high quality mev ultrafast electron diffraction", Rev. Sci. Instrum. **80**, 8, 083303 (2009).

Li, R. K., K. G. Roberts, C. M. Scoby, H. To and P. Musumeci, "Nanometer emittance ultralow charge beams from rf photoinjectors", Phys. Rev. ST Accel. Beams **15**, 090702, URL `https://link.aps.org/doi/10.1103/PhysRevSTAB.15.090702` (2012).

Li, W. H., C. J. R. Duncan, M. B. Andorf, A. C. Bartnik, E. Bianco, L. Cultrera, A. Galdi, M. Gordon, M. Kaemingk, C. A. Pennington, L. F. Kourkoutis, I. V. Bazarov and J. M. Maxson, "A kiloelectron-volt ultrafast electron micro-diffraction apparatus using low emittance semiconductor photocathodes", Struct. Dyn. **9**, 2, 024302, URL `https://doi.org/10.1063/4.0000138` (2022).

Manini, P. and E. Maccallini, "NEG pumps: Sorption mechanisms and applications", in "CERN Course on Vacuum for Particle Accelerators", (2017).

Manz, S., A. Casandruc, D. Zhang, Y. Zhong, R. A. Loch, A. Marx, T. Hasegawa, L. C. Liu, S. Bayesteh, H. Delsim-Hashemi *et al.*, "Mapping atomic motions with ultrabright electrons: towards fundamental limits in space-time resolution", Faraday Discussions **177**, 467–491 (2015).

Martinelli, R. U., "Effects of cathode bumpiness on the spatial resolution of proximity focused image tubes", Appl. Opt. **12(8)**, 1841–1845 (1973).

Mass Finishing, Inc., "1/2" x 5/8" dura 30 cone", URL `https://massfin.com/shop/ceramic-media/ceramic-cone-media/1-2-x-5-8-dura-30-cone/`, 5500-10320 (2022a).

Mass Finishing, Inc., "1/2" x 9/16" sx cone", URL `https://massfin.com/shop/synthetic-cone-media/1-2-x-9-16-sx-cone/`, 5500-10370 (2022b).

Mass Finishing, Inc., "Ts compound- 5 gallon bucket", URL `https://massfin.com/shop/chemical-compounds/t-s-compound-5-gallon-bucket/`, 5400-10002 (2022c).

Maxson, J., I. Bazarov, B. Dunham, J. Dobbins, X. Liu and K. Smolenski, "Design, conditioning, and performance of a high voltage, high brightness dc photoelectron gun with variable gap", Rev. Sci. Instrum. **85**, 9, 093306 (2014).

Maxson, J., I. Bazarov, W. Wan, H. Padmore and C. Coleman-Smith, "Fundamental photoemission brightness limit from disorder induced heating", New Journal of Physics **15**, 10, 103024 (2013).

Maxson, J., P. Musumeci, L. Cultrera, S. Karkare and H. A. Padmore, "Ultrafast laser pulse heating of metallic photocathodes and its contribution to intrinsic emittance", Nuc. Instrum. Meth. A **865**, 99 (2016).

Melitz, W., J. Shena, A. C. Kummela and S. Lee, "Kelvin probe force microscopy and its application", Surf. Scie. Rep. **66**, 1 (2011).

Miller, M. and E. Kenik, "Atom probe tomography: A technique for nanoscale characterization", Microscopy and Microanalysis **10**, 3, 336–341 (2004).

Montag, C., E. Aschenauer, G. Bassi, J. Beebe-Wang, S. Benson, J. Berg, M. Blaskiewicz, A. Blednykh, J. Brennan, S. Brooks, K. Brown, Y. Cai, Z. Conway, K. Deitrick, K. Drees, A. Fedotov, W. Fischer, C. Folz, D. Gassner, E. Gianfelice-Wendt, J. Grames, X. Gu, C. Gulliford, R. Gupta, Y. Hao, A. Hershcovitch, C. Hetzel, G. Hoffstaetter, D. Holmes, H. Huang, W. Jackson, J. Kewisch, Y. Li, F. Lin, C. Liu, H. L. III, Y. Luo, M. Mapes, D. Marx, G. McIntyre, T. Michalski, M. Minty, V. Morozov, F. Méot, S. Nayak, E. Nissen, Y. Nosochkov, R. Palmer, B. Parker, S. Peggs, B. Podobedov, J. Preble, V. Ptitsyn, V. Ranjbar, R. Rimmer, G. Robert-Demolaize, T. Satogata, S. Seletskiy, A. Seryi, V. Smaluk, K. Smith, G. Stupakov, M. Sullivan, S. Tepikian, R. Than, P. Thieberger, D. Trbojevic, N. Tsoupas, J. Tuozzolo, J. Unger, S. Verdú-Andrés, E. Wang, D. Weiss, F. Willeke, M. Wiseman, H. Witte, W. Wittmer, Q. Wu, D. Xu, W. Xu, A. Zaltsman, W. Zhang and Y. Zhang, "Design Status Update of the Electron-Ion Collider", in "Proc. IPAC'21", No. 12 in International Particle Accelerator Conference, pp. 2585–2588 (JACoW Publishing, Geneva, Switzerland, 2021).

Murooka, Y., N. Naruse, S. Sakakihara, M. Ishimaru, J. Yang and K. Tanimura, "Transmission-electron diffraction by mev electron pulses", Appl. Phys. Lett. **98**, 25, 251903 (2011).

Musumeci, P., J. Giner Navarro, J. Rosenzweig, L. Cultrera, I. Bazarov, J. Maxson, S. Karkare and H. Padmore, "Advances in bright electron sources", Nucl. Instrum. Methods Phys. Res., Sect. A **907**, 209–220, URL `https://www.sciencedirect.com/science/article/pii/S0168900218303541`, advances in Instrumentation and Experimental Methods (Special Issue in Honour of Kai Siegbahn) (2018).

Musumeci, P., J. Moody, C. Scoby, M. Gutierrez and M. Westfall, "Laser-induced melting of a single crystal gold sample by time-resolved ultrafast relativistic electron diffraction", Appl. Phys. Lett. **97**, 6, 063502 (2010).

Nagai, R., R. Hajima, N. Nishimori, T. Muto, M. Yamamoto, Y. Honda, T. Miyajima, H. Iijima, M. Kuriki, M. Kuwahara *et al.*, "High-voltage testing of a 500-kv dc photocathode electron gun", Rev. Sci. Instrum. **81**, 3, 033304 (2010).

Nangoi, J. K., S. Karkare, R. Sundararaman, H. A. Padmore and T. A. Arias, "Importance of bulk excitations and coherent electron-photon-phonon scattering in photoemission from pbte(111): Ab initio theory with experimental comparisons", Phys. Rev. B **104**, 115132, URL `https://link.aps.org/doi/10.1103/PhysRevB.104.115132` (2021).

National Academies of Sciences, Engineering, and Medicine, *An assessment of US-based electron-ion collider science* (National Academies Press, 2018).

Oudheusden, van, T., *Electron source for sub-relativistic single-shot femtosecond diffraction*, Ph.D. thesis, Applied Physics (2010).

Parzyck, C. T., A. Galdi, J. K. Nangoi, W. J. I. DeBenedetti, J. Balajka, B. D. Faeth, H. Paik, C. Hu, T. A. Arias, M. A. Hines, D. G. Schlom, K. M. Shen and J. M. Maxson, "Single-crystal alkali antimonide photocathodes: High efficiency in the ultrathin limit", Phys. Rev. Lett. **128**, 114801, URL `https://link.aps.org/doi/10.1103/PhysRevLett.128.114801` (2022).

Pellegrini, C., "The history of x-ray free-electron lasers", Eur. Phys. J. H **37**, 5, 659–708 (2012).

Pomarico, E., Y.-J. Kim, F. J. G. De Abajo, O.-H. Kwon, F. Carbone and R. M. Van Der Veen, "Ultrafast electron energy-loss spectroscopy in transmission electron microscopy", Mrs Bulletin **43**, 7, 497–503 (2018).

Precision Sapphire Technologies, Ltd., "Sapphire tubes, rods, spheres and special shapes", URL `https://www.sapphire.lt/products/tubes.shtml` (2022).

Rosenzweig, J., A. Cahill, B. Carlsten, G. Castorina, M. Croia, C. Emma, A. Fukusawa, B. Spataro, D. Alesini, V. Dolgashev, M. Ferrario, G. Lawler, R. Li, C. Limborg, J. Maxson, P. Musumeci, R. Pompili, S. Tantawi and O. Williams, "Ultra-high brightness electron beams from very-high field cryogenic radiofrequency photocathode sources", Nucl. Instrum. Methods Phys. Res., Sect. A **909**, 224–228, URL `https://www.sciencedirect.com/science/article/pii/S0168900218300780`, 3rd European Advanced Accelerator Concepts workshop (EAAC2017) (2018).

Rosenzweig, J. B., N. Majernik, R. R. Robles, G. Andonian, O. Camacho, A. Fukasawa, A. Kogar, G. Lawler, J. Miao, P. Musumeci, B. Naranjo, Y. Sakai, R. Candler, B. Pound, C. Pellegrini, C. Emma, A. Halavanau, J. Hastings, Z. Li, M. Nasr, S. Tantawi, P. Anisimov, B. Carlsten, F. Krawczyk, E. Simakov, L. Faillace, M. Ferrario, B. Spataro, S. Karkare, J. Maxson, Y. Ma, J. Wurtele, A. Murokh, A. Zholents, A. Cianchi, D. Cocco and S. B. van der Geer, "An ultra-compact x-ray free-electron laser", New J. Phys. **22**, 9, 093067, URL `https://doi.org/10.1088/1367-2630/abb16c` (2020).

Ruan, C.-Y., V. A. Lobastov, R. Srinivasan, B. M. Goodson, H. Ihee and A. H. Zewail, "Ultrafast diffraction and structural dynamics: The nature of complex molecules far from equilibrium", Proc. Natl. Acad. Sci. U.S.A. **98**, 13, 7117–7122 (2001).

Ruska, E., "Zur fokussierbarkeit von kathodenstrahlbündeln großer ausgangsquerschnitte", Zeitschrift für Physik **83**, 9-10, 684–697 (1933).

Ruth, R. D., "A canonical integration technique", IEEE Trans. Nucl. Sci. **30**, CERN-LEP-TH-83-14, 2669–2671 (1983).

SAES Getters S.p.A., "Nextorr neg - ion combination pump", URL `https://www.saesgetters.com/products/nextorr-pumps` (2022).

Saha, P., O. Chubenko, G. S. Gevorkyan, A. Kachwala, C. J. Knill, C. Sarabia-Cardenas, E. Montgomery, S. Poddar, J. T. Paul, R. G. Hennig, H. A. Padmore and S. Karkare, "Physically and chemically smooth cesium-antimonide photocathodes on single crystal strontium titanate substrates", Appl. Phys. Lett. **120**, 19, 194102, URL `https://doi.org/10.1063/5.0088306` (2022).

Sannibale, F., D. Filippetto, C. F. Papadopoulos, J. Staples, R. Wells, B. Bailey, K. Baptiste, J. Corlett, C. Cork, S. De Santis, S. Dimaggio, L. Doolittle, J. Doyle, J. Feng, D. Garcia Quintas, G. Huang, H. Huang, T. Kramasz, S. Kwiatkowski, R. Lellinger, V. Moroz, W. E. Norum, H. Padmore, C. Pappas, G. Portmann, T. Vecchione, M. Vinco, M. Zolotorev and F. Zucca, "Advanced photoinjector experiment photogun commissioning results", Phys. Rev. ST Accel. Beams **15**, 103501, URL `https://link.aps.org/doi/10.1103/PhysRevSTAB.15.103501` (2012).

Scienta Omicron GmbH, "Flag style sample plate tribus spm (molybdenum) set of 3", URL `https://scientaomicron.com/`, pN07178-S (2023).

Seyler, K. L., P. Rivera, H. Yu, N. P. Wilson, E. L. Ray, D. G. Mandrus, J. Yan, W. Yao and X. Xu, "Signatures of moiré-trapped valley excitons in mose2/wse2 heterobilayers", Nature **567**, 7746, 66–70 (2019).

Siegel, R., *Thermal radiation heat transfer* (CRC press, 2001).

Siggins, T., C. Sinclair, C. Bohn, D. Bullard, D. Douglas, A. Grippo, J. Gubeli, G. Krafft and B. Yunn, "Performance of a dc gaas photocathode gun for the jefferson lab fel", Nucl. Instrum. Methods Phys. Res., Sect. A **475**, 1, 549–553, URL `https://www.sciencedirect.com/science/article/pii/S0168900201015960` (2001).

Spence, J. and M. Howells, "Synchrotron soft x-ray and field-emission electron sources: a comparison", Ultramicroscopy **93**, 3, 213–222, URL `https://www.sciencedirect.com/science/article/pii/S0304399102002784`, special issue in Honour of Peter W. Hawkes on the Occasion of his 65th Birthday, in Recognition of his Contributions to Electron Optics and Electron Microscopy (2002).

Stoffel, N. and P. Johnson, "A low-energy high-brightness electron gun for inverse photoemission", Nucl. Instrum. Methods Phys. Res., Sect. A **234**, 2, 230–234 (1985).

Stäubli International AG, "Multilam technology and products", URL `https://www.staubli.com/global/en/electrical-connectors/products/multilam-products-and-technology.html` (2019).

Swope, W. C., H. C. Andersen, P. H. Berens and K. R. Wilson, "A computer simulation method for the calculation of equilibrium constants for the formation of physical clusters of molecules: Application to small water clusters", J. Chem. Phys. **76**, 648 (1982a).

Swope, W. C., H. C. Andersen, P. H. Berens and K. R. Wilson, "A computer simulation method for the calculation of equilibrium constants for the formation of physical clusters of molecules: Application to small water clusters", The Journal of chemical physics **76**, 1, 637–649 (1982b).

Technology Applications, Inc., "Cryocooler series (cs) cuts thermal straps for cryocoolers / cryorefrigerators", URL `https://www.techapps.com/cryocooler-series-thermal-straps` (2022).

Tran, K., G. Moody, F. Wu, X. Lu, J. Choi, K. Kim, A. Rai, D. A. Sanchez, J. Quan, A. Singh *et al.*, "Evidence for moiré excitons in van der waals heterostructures", Nature **567**, 7746, 71–75 (2019).

van der Geer, S. and M. de Loos, "Applications of the general particle tracer code", in "Proceedings of the 1997 Particle Accelerator Conference (Cat. No.97CH36167)", vol. 2, pp. 2577–2579 vol.2 (1997).

Van Oudheusden, T., E. De Jong, S. Van der Geer, W. O. 't Root, O. Luiten and B. Siwick, "Electron source concept for single-shot sub-100 fs electron diffraction in the 100 kev range", J. Appl. Phys. **102**, 9, 093501 (2007).

Van Oudheusden, T., P. Pasmans, S. Van Der Geer, M. De Loos, M. Van Der Wiel and O. Luiten, "Compression of subrelativistic space-charge-dominated electron bunches for single-shot femtosecond electron diffraction", Phys. Rev. Lett. **105**, 26, 264801 (2010).

Vecchione, T., D. Dowell, W. Wan, J. Feng and H. Padmore, "Quantum efficiency and transverse momentum from metals", Proc. of FEL2013 pp. p–424 (2013).

Wang, X., P. Musumeci, E. Lessner and J. Goldstein, "Report of the basic energy sciences workshop on the future of electron sources, september 8-9, 2016", DOE Technical Report URL `https://www.osti.gov/biblio/1616511` (2016).

Wang, X., D. Xiang, T. Kim and H. Ihee, "Potential of femtosecond electron diffraction using near-relativistic electrons from a photocathode rf electron gun", J. Korean Phys. Soc. **48**, 3, 390 (2006).

Weathersby, S., G. Brown, M. Centurion, T. Chase, R. Coffee, J. Corbett, J. Eichner, J. Frisch, A. Fry, M. Gühr *et al.*, "Mega-electron-volt ultrafast electron diffraction at slac national accelerator laboratory", Rev. Sci. Instrum. **86**, 7, 073702 (2015).

Witte, H., J. Adam, M. Anerella, E. Aschenauer, J. Berg, M. Blaskiewicz, A. Blednykh, W. Christie, J. Cozzolino, K. Drees, B. Gamage, D. Gassner, K. Hamdi, C. Hetzel, H. Hocker, D. Holmes, A. Jentsch, A. Kiselev, P. Kovach, H. L. III, Y. Luo, G. Mahler, A. Marone, G. McIntyre, T. Michalski, C. Montag, V. Morozov, R. Palmer, B. Parker, S. Peggs, S. Plate, V. Ptitsyn, G. Robert-Demolaize, C. Runyan, J. Schmalzle, K. Smith, M. Stutzman, M. Sullivan, S. Tepikian, P. Thieberger, J. Tuozzolo, F. Willeke, W. Wittmer, Q. Wu and Z. Zhang, "The Interaction Region of the Electron-Ion Collider EIC", in "Proc. IPAC'21", No. 12 in International Particle Accelerator Conference, pp. 2574–2577 (JACoW Publishing, Geneva, Switzerland, 2021).

Xiang, D., W. Huang, Y. Du, L. Yan, R. Li, C. Tang and Y. Lin, "First principle measurements of thermal emittance for copper and magnesium", Proc. of PAC07 p. 1049 (2007).

Xie, J., M. Demarteau, R. Wagner, S. Schubert, M. Gaowei, K. Attenkofer, J. Walsh, J. Smedley, J. Wong, J. Feng, H. A. Padmore *et al.*, "Synchrotron x-ray study of a low roughness and high efficiency k_2cssb photocathode during film growth", J. Appl. Phys. **50**, 205303 (2017).

XP Power, "Os series", URL `https://www.xppower.com/product/OS-Series?m=OS250N08.0` (2022).

Yoshida, H., "Construction of higher order symplectic integrators", Physics letters A **150**, 5-7, 262–268 (1990).

Zewail, A. H., "4d ultrafast electron diffraction, crystallography, and microscopy", Annu. Rev. Phys. Chem. **57**, 65–103 (2006).

Zhang, Z. and C. Tang, "Analytical study on emittance growth caused by roughness of a metallic photocathode", Phys. Rev. Spec. Top. - A.B. **18**, 053401 (2015).

APPENDIX A

DISCLAIMER

The work presented in chapter 2 was originally published as Gevorkyan et al. (2018). The work presented in chapter 3 and is a manuscripts that is currently under preparation with plans to submit to a journal, and has been published in conference proceedings as Gevorkyan et. al (2019,2022). The work presented in chapter 4 has been submitted as a manuscript to be published as Gevorkyan et. al. (2023). The work presented in chapter 5 has been published in the IPAC 2023 conference as Gevorkyan et al. (2023), which was submitted as a proceeding with joint coauthorship between Carlos Sarabia Cardenas and myself. I have obtained permission from all coauthors of these works to submit the contents of the publications as chapters of this dissertation.